

Vortex transition and thermal mixing by pitching a perforated flexible panel

Yicong Fu,^{1,*} Zhengyang Liu,² Samir Tandon,² Jake Gelfand,³ and Sunghwan Jung^{2,†}

¹*Sibley School of Mechanical and Aerospace Engineering,*

Cornell University, Ithaca, New York 14853, USA

²*Department of Biological and Environmental Engineering,*

Cornell University, Ithaca, New York 14853, USA

³*Department of Biological Sciences, Cornell University, Ithaca, New York 14853, USA*

(Dated: April 8, 2025)

The effective transport of heat and mass is crucial to both industrial applications and physiological processes. Recent research has evaluated the benefit of using flexible reeds for triggering the vortex induced vibration to enhance mixing, as opposed to traditional techniques like rigid blender or static meshes. Inspired by the soft, porous, and moving fish gill lamellae, we proposed a new concept of thermal dispenser that prescribes active pitching motion to the leading edge of an otherwise passively flapping perforated panel. Experimental measurements revealed drastic differences between the steady leaky flow wake behind a statically deflected perforated panel and the periodic shedding wakes with complex vortex structure transitions behind an actuated perforated panel with or without chord-wise flexibility. A semi-empirical simulation of the thermal convection and diffusion takes the experimentally obtained velocity as input and yields the temperature results. Vortex dynamics, Lagrangian coherent structures, and thermal mixing behaviors were analyzed and compared to elucidate the effects of kinematics, perforation, and flexibility on the wake mode transitions, lateral entrainment mixing, and overall heating. Our work provides a foundational understanding of the fluid-structure interactions of perforated bendable panels under active control which has not been described before in the intermediate Reynolds number range. It provides insights for developing an innovative bio-inspired heat or mass dispenser potentially suitable for subtle and small scale applications.

Keywords: flexible vortex generator, perforated panel, thermal mixing, vortex transition, Lagrangian coherent structure, pitching

* To whom correspondence should be addressed.

E-mail: yf357@cornell.edu.

Address: B45 Riley Robb Hall, 111 Wing Drive, Ithaca, New York 14853, USA.

Phone: 434-466-7151.

† To whom correspondence should be addressed.

E-mail: sj737@cornell.edu.

I. INTRODUCTION

The material and thermal transport is a ubiquitous phenomenon governed by the convection and diffusion with crucial applications in both human technologies and biological activities, such as wastewater management [1, 2], temperature regulation [3, 4], blood dialysis [5], respiration [6], predation [7, 8], and chemical communications [9–11]. Tremendous research efforts has been put into the development of effective fluid mixing from microfluidic channels [12, 13] to large turbulent eddies [14, 15]. Within the laminar flow regime, a major obstacle for mixing is the boundary layer formed due to the viscous no-slip condition at the solid-fluid interface.

Passive mixers have been proposed and used in many situations. Rigid vortex generators including protrusions and dimples on the surface can lead to the formation of vortices and turbulence that encourages mixing between the bulk and the boundary layer [16–22]. However, the rigid vortex generators are known to significantly increase the pressure losses due to higher surface friction and geometric anomalies, requiring more energy consumption to maintain the desired flow rate. In recent years, flexible vortex generators have received much attention as a potential replacement for the rigid counterparts. By tuning the size [23], flexural rigidity [24–26], mass distribution [27], attachment condition [28, 29], and array placement [30–32], the vortical flow downstream of the flexible reed can significantly enhance the thermal mixing and local Nusselt number (Nu) in the case of boundary heating and cooling. It has been reported that the passively mounted flexible reed generally fall in three kinematic categories in response to the hydrodynamic forces: static reconfiguration, vortex induced vibration (VIV), and lodging [33]. Static reconfiguration occurs when the hydrodynamic forces are relatively small and steady due to the absence or weak formation of vortices. They behave similar to rigid panels since material deformation is minor and motion is negligible. VIV occurs when the vortices periodically shed from the edge of the reed at a certain frequency that locks in with the vibrational frequency of the solid structure. This mode generates much stronger and coherent vortices that contribute to the overall mixing. Lodging happens when the hydrodynamic forces completely push the flexible reed against the solid wall so that the resulting shape acts like a stationary hump. The limitations of passive flexible vortex generators are obvious. Their efficacy necessitates the occurrence of VIV, which is strongly dependent on the flow condition, resonance of the solid structure, and mounting boundary conditions, restraining the versatility of their applications. The passive nature still drains mechanical energy from the flow and result in pressure loss.

Active mixing, on the other hand, has a wider application potential thanks to the conscious manipulation of the fluid flow, despite the drawback of energy consumption. Many examples exist in nature, including fish gill respiration [34], insect wing-beat-induced odor capture [35, 36], honey bee hive’s active ventilation

[37], cilia pumping [38], cytoplasmic streaming [39], etc. Many bio-inspired devices have been made to mimic the coordinated motions of rigid and flexible structures [40–45]. Experiments and simulations have shown their promising capabilities of material transport and mixing. In the context of gradient-driven flow, the concept of dynamic filtration has been proposed as a means to maintain high filtration flux across semi-permeable membranes by preventing membrane fouling with increased shear stresses [46]. In this work, we take inspiration from fish gill’s active pumping respiration and integrate key features into our engineering model. Fish gill filaments form a mesh-like structure by the primary lamellae and the perpendicularly standing secondary lamellae. They have large surface areas and rich capillary vessels for metabolic exchange between blood and surrounding water [34]. Depending on the mechanism of water intake (ram ventilation or operculum pumping), gill filaments are found to have different degrees of calcification to fine tune the rigidity such that hydrodynamic forces do not create non-respiratory shunting flows [47, 48]. Dissections of the fish gills also identified abductor and adductor muscles attached to the filaments that allow active control of lateral motions [34]. Though complex, the key features of fish gill filaments can be reduced to three parameters: porosity, flexibility, and motion. Thus, we incorporated all three into our proposed thermal dispenser: a pitching perforated panel with chord-wise flexibility.

The fluid structure interactions (FSI) of actuated hydrofoils have received extensive research in the context of vortex formation, propulsion, and fluid pumping. Fish inspired oscillatory and undulatory swimming was thoroughly summarized by Smits [49]. Investigations in the dimensionless range of fish locomotion have reported a 2-pair (2P) to 2-single (2S) wake structure transition as a function of the amplitude-defined Strouhal number ($St_A = Af/U_\infty$), dimensionless wavelength ($\lambda^* = \lambda/c$), and aspect ratios (AR) [50–53]. Here, A is the oscillation amplitude, f is the oscillation frequency, U_∞ is the characteristic incoming flow velocity, λ is the solid deformation wavelength, and c is the chord length. Schnipper *et al.* [54] adopted 2D assumption in a soap film experiment with pitching rigid foil at the leading edge and summarized a phase map for wake transitions from 2S von Karman wake to 8P wake as a function of the dimensionless amplitude ($A_D = A/d$) and foil-thickness(d)-defined Strouhal number ($St_D = df/U_\infty$), which can be combined as the amplitude-defined Strouhal number St_A . As a consequence of the wake vortex structure change, mean velocity streaming, force generation, hydrodynamic power consumption, and hydrodynamic efficiency were analyzed, but few has considered the thermal mixing benefit of these vortex structures. Recent research has also started to examine more complicated conditions of the foils such as irregular planform shapes [55], trailing edge (TE) tapers [56], surface roughness [57], and leaky surfaces [58–61]. Particularly, leaky foils with perforations or bristle structures have raised huge interest among biomimetic engineers due to their outstanding performances in certain fluid and kinematic conditions. Statically positioned perforated flexible panels in cross flow have been reported to reduce drag and flexural rigidity (EI), and thus stabi-

lize at a more-deformed reconfiguration angle than non-perforated panels [62, 63]. Clap-and-fling flight of small insects with bristled wings also revealed the benefit of drag reduction without significantly sacrificing lift [64, 65]. In this work, we incorporate perforation, material flexibility, and prescribed motion to the FSI. We aim to characterize the different vortex shedding mechanisms and thermal mixing effects, potentially opening a new avenue for bio-inspired heat and mass dispensing system design.

II. EXPERIMENTAL METHODS

A. Apparatus fabrication

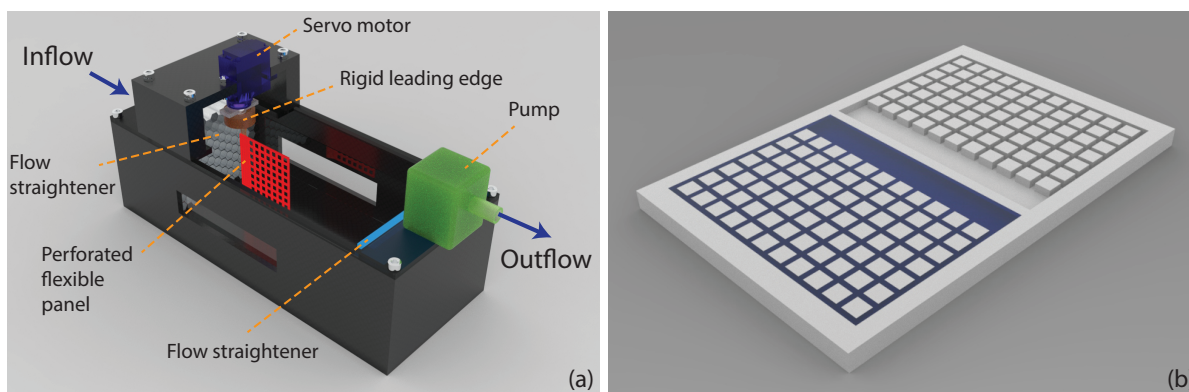


FIG. 1. **Experimental apparatus rendered in Luxion Keyshot.** (a) In-house designed and fabricated flow channel. (b) Silicone mold of the perforated flexible panel. One side is filled with silicone (blue) and the other side is empty.

We designed and fabricated a low-cost fluid channel (FIG. 1(a)) capable of creating uniform, steady, and laminar background flows at different Reynolds numbers (Re). A Bambu Lab P1P 3D-printer was used to print polylactic acid (PLA) with FDM method. A rectangular channel of $186 \times 76 \times 54$ mm (test section $90 \times 70 \times 50$ mm; length \times width \times height) supports an overhanging mount for motors above the interface. A 30 mm thick honeycomb straightener with an average hole diameter of 5 mm was placed upstream to laminarize the inflow. A 3D-printed PLA straightener was placed downstream to further laminarize the fluid flow prior to the outflow sink. A 12 volt DC water pump was connected to the downstream straightener to generate flow. Two clear polycarbonate sheet (McMaster Carr) windows were cut open through the side walls of the channel to allow illumination. The channel was positioned in a larger fish tank with water filled to the upper edge of the channel. The water pump drew water from inside the channel and recirculated it in the fish tank. Outside the channel, plastic meshes were placed around the pump exit and the channel inlet as dampers to absorb the vibrations. An MG90S micro servo motor is mounted over the flow channel to actuate pitching motion about the center axis of the motor shaft. A 3D printed PLA rigid shaft extended

vertically downward from the motor shaft to attach the perforated panels.

Two perforated panels with the same dimensions but different flexural rigidities (EI) were fabricated. The panel had an overall rectangular shape with a 45 mm span (s) and a 34.5 mm chord (c). Along the chord, 7 square perforation holes of $a \times a = 3 \times 3$ mm size were separated by $b = 1$ mm solid posts. Along the span, the chord-wise hole arrays were linearly repeated 11 times with $b = 1$ mm separations to result in a total of 77 perforation holes. The rigid panel was 3D printed with PLA. The flexible panel was casted with MoldStar 31T silicone rubber (SmoothOn Inc.) in a 3D printed PLA mold (FIG. 1(b)). Both panels were 0.75 mm thick. From the same dimension, the second moment of area (I) is the same for both panels. The Young's modulus (E) is 2750 ± 160 MPa for PLA and approximately 2 MPa for silicone of A30 shore hardness. The EI would have three orders of magnitude difference, hence the naming "flexible" and "rigid". After fabrication, the panel's non-perforated side is fused to the rigid shaft from the motor as the leading edge (LE).

B. Particle image velocimetry

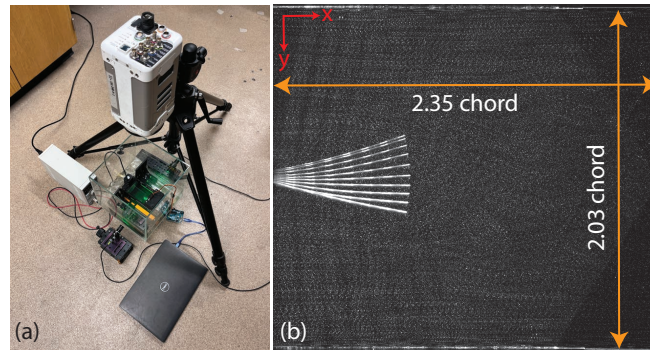


FIG. 2. **Particle image velocimetry.** (a) Experimental setup showing the relative positions of the flow channel, high-speed camera, continuous laser sheets, and Arduino Uno microcontroller. (b) Overlaid every 10th image of one downstroke of the perforated flexible panel pitching at $f = 0.64$ Hz, showing the DPIV domain size.

2D digital particle image velocimetry (DPIV) was performed to capture the fluid velocity field in the experimental setup as FIG. 2(a). One Class IIIB laser (LaserLand) was placed on each side of the channel to create a shadowless horizontal sheet shining through the windows. A NOVA S6 Photron high-speed camera was positioned vertically downward above the test section to capture the fluid motion at 125 frames per second (FPS) through the PFV4 software. Channel was filled with DI water and seeded with Dantec silver-coated hollow glass spheres ($10 \mu\text{m}$). The recording domain is defined as $2.03 c$ wide and $2.35 c$ long, containing all the perforation holes and separation posts (FIG. 2(b)).

Without putting anything in the test section, we confirmed the background flow to be uniform, steady,

and laminar. An overlay of the DPIV images (FIG. 3(a)) reveal the pathlines of the seeding particles to follow the laminar streaks from left to right. DPIV results from two extreme flow speed cases (FIG. 3(b-c)) show consistently reliable flow fields with a wide uniform flow profile with relatively small boundary layers near the wall.

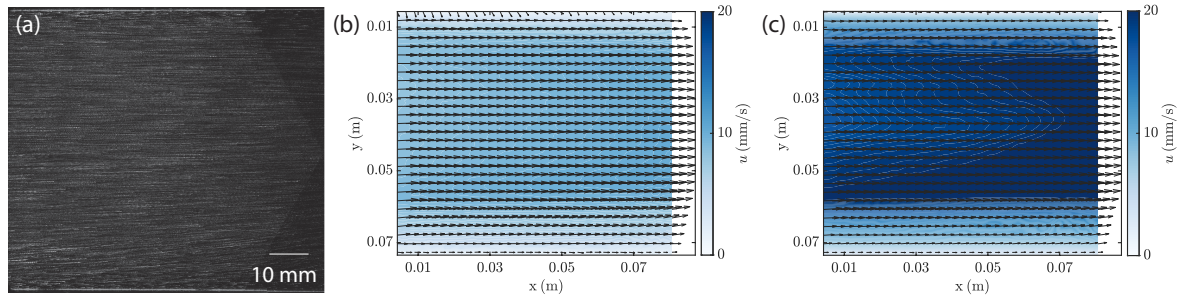


FIG. 3. **Uniform and steady laminar flow.** (a) Laser-illuminated neutrally buoyant particle pathlines over 1 second. (b) Velocity field at 4 VDC Pump speed. (c) Velocity field at 12 VDC Pump speed.

During experiments with the panel, the laser sheet's height was adjusted to align with the perforation holes at the center of the span. This helps visualize all the fluid flow penetrating through the perforation and guarantees negligible 3D effects from the top and bottom edges. The pump was set to 12 VDC, which creates an averaged flow speed of 17 mm/s equivalent to a fixed $Re = \rho U_{\infty} c / \mu$ of 590. Either panel was pitched about the leading edge at a frequency f ranging from 0.64 to 1.14 Hz. For every condition, a minimum 2 min wait time was given before starting recording to guarantee the flow stabilized to a repeating pattern without effects from the previous condition or external sources. For steady flow fields without solid structures or with a static structure, 8 s (1000 frames) was recorded. For unsteady flow fields around the pitching panel, 10 stroke cycles were recorded to extract the phase-averaged velocity to multiple frames. Image postprocessing were done in ImageJ, including outlier removal, de-speckling, contrast enhancement, background subtraction, and binarization, to generate the masks for the solid structures in the DPIV video. DPIV analysis were performed in PIVlab version 2.63 [66] in MATLAB 2024b on the raw video, with masks overlaid. With a 2-layer interrogation window and a 50% stepping, we achieved 10×10 px velocity field resolution from the 1024×1024 px image resolution.

III. COMPUTATIONAL METHODS

A. Convection Diffusion Equation

Due to the difficulty of experimentally fabricating a thermal couple or a heat exchanger of this shape and flexibility, we decided to adopt a semi-empirical computation method to simulate the thermal mixing by using the experimental flow field as an input. Conventionally, full computational fluid dynamics (CFD) methods for the present scenario would require the integration of three governing physics: fluid motion, solid deformation, and heat transfer. The first two are usually coupled as an iterative feedback loop since the fluid flow imposes hydrodynamic forces to the solid structure, and the deforming solid structure in turn dictates the motion of the fluid. Such computational FSI has been well established to study flexible vortex generators [30, 61, 67]. However, the FSI is usually computationally decoupled from the heat transfer simulations which is based on the Convection Diffusion equation

$$\frac{\partial T}{\partial t} = D \nabla^2 T - \mathbf{u} \cdot \nabla T. \quad (1)$$

Here, T is the fluid temperature, t is time, $\mathbf{u} = [u, v]$ is the 2D fluid velocity vector, and D is the thermal diffusivity of water taken as $1.43 \times 10^{-7} \text{ m}^2/\text{s}$. Since the DPIV experiments essentially provide the same \mathbf{u} information as the direct numerical solutions from an FSI solver, we believe that this semi-empirical method is able to yield meaningful and accurate results on thermal mixing.

B. Simulation settings and validations

The preparation for the thermal simulation starts from pre-processing the experimental velocity field and solid structure positions. For steady flow fields with static solid structures in water, no velocity averaging was performed. The raw velocity fields across 1000 frames were repeated 4 times to extend the simulation time to 32 seconds, which is enough to reach a steady-state equilibrium solution. For unsteady flow fields around the pitching panel, phase-averaged velocity fields were extracted from 10 recorded stroke cycles and repeated N times such that the total simulation time also extends to about 32 seconds. Here, N is equivalent to the number of phase-averaged stroke cycles simulated. Similarly, the solid structure position for a static object is extracted from images, mapped to the same meshgrid as the velocity field, and kept unchanged throughout the simulation. The solid structure positions of the moving and deforming panels were extracted from the phase-averaged frames, mapped to the velocity meshgrids, and repeated N times.

In this work, we assume that the solid structure immersed in the fluid is not only a vortex generator but also the heat source responsible for increasing the fluid temperature. We artificially impose a Dirichlet constant T boundary condition across the background flow inlet (left) at $T_\infty = 300$ K at all times. This intuitively simulates the condition of a one-directional flow through a pipeline section at a constant source temperature. We also impose another Dirichlet constant T boundary condition at the solid structure heat sources at $T_s = 350$ K. Thus, the maximum temperature difference is $\Delta T = 50$ K. At the top, bottom, and outlet (right) boundaries, we impose Neumann constant flux boundary conditions, $\partial T / \partial \mathbf{n} = 0$, with \mathbf{n} being the outward normal vector at each boundary surface. The interior nodes are computed based on the temperature and velocity information of their adjacent nodes. Specifically, ∇T of the interior nodes follow the first order upwind scheme, as

$$\left(\frac{\partial T}{\partial x}\right)_{i,j} \approx \begin{cases} \frac{T_{i,j} - T_{i-1,j}}{\Delta x}, & \text{if } u_{i,j} > 0 \\ \frac{T_{i+1,j} - T_{i,j}}{\Delta x}, & \text{if } u_{i,j} < 0 \end{cases} \quad (2a)$$

$$\left(\frac{\partial T}{\partial y}\right)_{i,j} \approx \begin{cases} \frac{T_{i,j} - T_{i,j-1}}{\Delta y}, & \text{if } v_{i,j} > 0 \\ \frac{T_{i,j+1} - T_{i,j}}{\Delta y}, & \text{if } v_{i,j} < 0 \end{cases} \quad (2b)$$

,

to prevent nonphysical oscillations in the computational results. $\nabla^2 T$ of the interior nodes follow the central difference scheme, as

$$\left(\frac{\partial^2 T}{\partial x^2}\right)_{i,j} \approx \frac{T_{i+1,j} - 2T_{i,j} + T_{i-1,j}}{\Delta x^2} \quad (3a)$$

$$\left(\frac{\partial^2 T}{\partial y^2}\right)_{i,j} \approx \frac{T_{i,j+1} - 2T_{i,j} + T_{i,j-1}}{\Delta y^2} \quad (3b)$$

.

Then, the remaining temperature gradient and Laplacian on the boundary nodes are simply extrapolated from the two adjacent interior nodes. The constructed $\partial T / \partial t$ matrix is then linearized to be integrated by MATLAB function ODE45 based on the explicit Runge-Kutta (4,5) formula [68, 69]. Simulation time domain is segmented based on the phase-averaged DPIV frames, making each segment 8 ms. Within each time segment, the integration time step sizes are automatically determined by ODE45, and only the temperature field at the end of the time segment is recorded as the result for the corresponding phase-averaged DPIV frame. Velocity fields within the time segment are linearly interpolated using the bounding fields. For the

first time segment, the initial condition is set to $T_s = 350$ K for all the solid structure nodes and $T = 300$ K for all the fluid nodes. For the following time segments, the previous recorded temperature field is then used as the initial condition for the next time segment to evolve the thermal mixing over time.

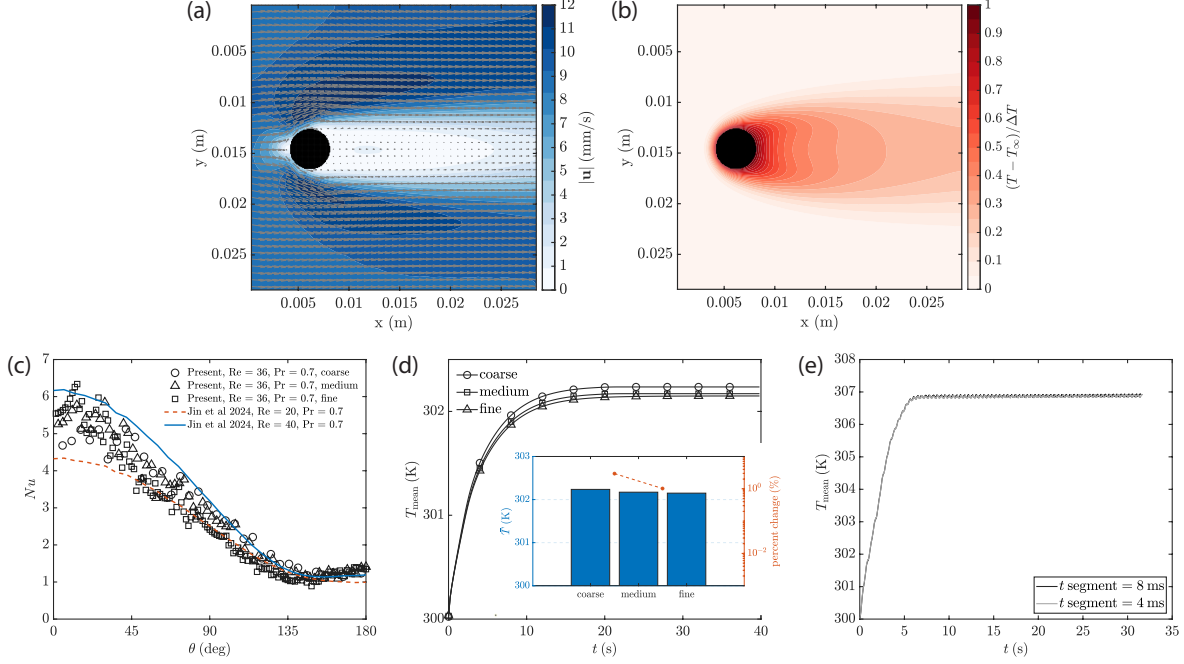


FIG. 4. **Solver validation results.** (a) time-averaged velocity field of the flow past cylinder at $Re = 36$. (b) Simulated temperature field for the flow past cylinder at $Re = 36$. (c) Nusselt number along the solid-fluid interface at the cylinder. Upper and lower semi-circles are averaged due to the symmetry. Our results are compared against published results by Jin *et al.* [27], with permission from the corresponding author. (d) Domain-averaged temperature evolution over time for different meshgrid sizes in flow past cylinder. Inset compares the equilibrium temperatures (blue) for three meshgrid sizes and the percent changes (orange) to confirm acceptable mesh size independence beyond “medium”. (e) Simulation time step size (t segment length) convergence verified with the flexible panel pitching at $f = 1.14$ Hz.

To validate the Convection Diffusion solver, we performed a canonical example of a forced convection by an isothermal circular cylinder in cross flow. We placed a 3D printed PLA circular cylinder with a 4 mm diameter (d) vertically in the middle of the test section with a constant U_∞ about 9 mm/s. Taking water density as $\rho = 1000$ kg/m³ and dynamic viscosity as $\mu = 1 \times 10^{-3}$ Pa \cdot s, the $Re = \rho U_\infty d / \mu$ is about 36. According to the dimensionless form of the Convection Diffusion equation,

$$\frac{\partial T^*}{\partial t^*} = \frac{1}{Pe} \nabla^{*2} T^* - \mathbf{u}^* \cdot \nabla^* T^*, \quad (4)$$

where Pe denotes the Peclet number and the $(\cdot)^*$ denotes the non-dimensionalization, we understand that both Re and the Prandtl number (Pr) characterize the physics since $Pe = RePr$. For a good comparison

with published results, similar dimensionless numbers are crucial for maintaining the dynamic similarity. Thus, we artificially set the thermal diffusivity to $1.43 \times 10^{-6} \text{ m}^2/\text{s}$ (one order higher than that of water) to force the Pr at 0.7. [This setting is only for validating the solver. The true thermal diffusivity of water is used in other simulations of the present work.] Due to the horizontal 2D assumption, we neglect buoyancy effects from the fluid density change with temperature and set the Grashof number (Gr) and Richardson number (Ri) to 0. This will be true for simulations for the pitching panels too.

As shown in FIG. 4(a), the steady recirculating twin vortex wake behind the cylinder at Re of 36 is consistent with previous reports [70]. Same simulation settings were applied, besides the isothermal condition on the cylinder is kept at $T_s = 320 \text{ K}$ ($\Delta T = 20 \text{ K}$). After reaching the steady-state solution, we examine the Nusselt number (Nu) along the semi-circle solid-liquid interface as an indicator for the ratio between heat convection and conduction, commonly used to validate simulations [27, 71, 72]. Based on the following equation [27],

$$Nu|_{\theta} = - \frac{D}{\Delta T} \left. \frac{\partial T}{\partial r} \right|_{\theta}, \quad (5)$$

we compute the Nu as a function of θ which is defined as 0° at the upstream stagnation center and positive in the clockwise direction. $\Delta T = 20 \text{ K}$ is the maximum temperature difference and $\partial T/\partial r$ is the radial temperature gradient along the solid surface at various θ angles. Our results in FIG. 4(b-c) show excellent agreement with published data, exhibiting the same magnitude and trend. For smaller θ , i.e. left half of the cylinder, Nu values are more scattered due to the compression of the velocity boundary layer and the incapability of DPIV to experimentally resolve thin velocity boundary layers or reflect the no-slip condition. As a result, the thermal boundary layer on the upstream side is also compressed to be thinner, leaving a sharper temperature gradient potentially causing the data scatter. Acknowledging the limitation of the experimental data, we still believe the Nu trend validates our solver's ability to study thermal mixing.

We also checked the meshgrid size independence threshold to reduce the computational cost while yielding converged results. The baseline mesh comes from the discretizations of the DPIV velocity field, which is inherently a Cartesian system. The baseline mesh size is about $d/12$. Linearly interpolating once, twice, and three times would result in smaller mesh sizes of $d/24$ (coarse), $d/48$ (medium), and $d/96$ (fine). All three mesh densities converged to highly similar results for the Nu and domain-averaged temperature (T_{mean}), as shown in FIG. 4(c-d). Here, T_{mean} is calculated as $\frac{1}{S} \int T dx dy$ where S is the area of the domain. As shown in the FIG. 4(d) inset, the percent change of the equilibrium temperature (\bar{T}) from coarse to medium mesh is 3% and from medium to fine mesh is 1%. Thus, we decided to use the medium mesh density (twice

interpolation) for all further simulations. Here, \bar{T} is calculated as $\frac{1}{\Delta t} \int T_{\text{mean}} dt$, where Δt is the time length for time-averaging.

We further checked the simulation time step size convergence. The way we setup the pitching panel simulation assumes that the solid structure heats up the fluid replenishing its previous position to the maximum temperature when it moves to the next position. This setting relies on the premise of large overlap of solid structure positions between adjacent frames. To confirm the recording FPS is sufficiently high and the solid structure displacement between adjacent simulation frames is sufficiently small, we tested two time segment lengths with the flexible panel pitching at $f = 1.14$ Hz. The aforementioned 8-ms time segment is halved to 4 ms. Simulation results from both matched very well, with \bar{T} reaching 306.894 K and 306.877 K respectively (FIG. 4(e)). This test case is at the highest frequency with the least anticipated solid structure overlap between adjacent frames. Therefore, we safely choose 8 ms as the time segment for further simulations.

IV. RESULTS

A. Static deflection at maximum pitch angle of 15°

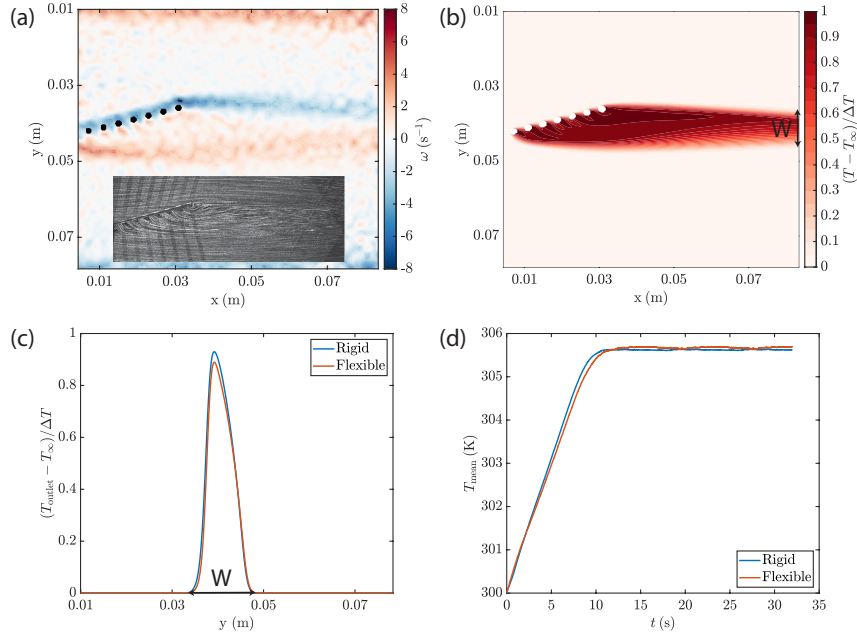


FIG. 5. **Statically positioned rigid and flexible panel at 15° show nearly identical results.** (a) Instantaneous vorticity field around the flexible panel. (b) Time-averaged equilibrium temperature field around the flexible panel. (c) Outlet temperature wake widths for both panels. (d) Simulated domain-averaged temperature evolution over time for both panels.

As a reference, we first position the panel at the maximum pitching angle (15°) without prescribing motion, thus naming it the “static” case. There is negligible difference between the rigid and flexible panels under this condition. The flexible panel experiences a very small hydrodynamic force due to the perforation letting water pass through, resulting in undetectable deformation compared with the rigid panel. No structural vibrations or periodic vortex shedding were seen, indicating that this belongs to the “lodging” regime, as reported in previous work [33]. For this steady flow field, we visualize the instantaneous vorticity and the formation of a low-velocity zone surrounded by shear layers (FIG. 5(a)). The time-averaged temperature field over the last 4 s of the simulation displayed little mixing in and outside the wake region due to insulation from the shear layers (FIG. 5(b)). The width of outlet thermal wake (W) was found to be nearly identical for both panels (FIG. 5(c)). Finally, the time evolution of T_{mean} reached \bar{T} at 305.7 K at around 11 s for both panels (FIG. 5(d)). Consistent thermal performances between two panels demonstrate the same fluid flow and mixing ability at this particular setting. As a baseline reference, their similarity guarantees the differences among later cases with prescribed motion are due to the different unsteady FSI of two panels. These results would help quantify how much performance boost takes place when the panels are actuated.

B. Kinematics of the pitching panels

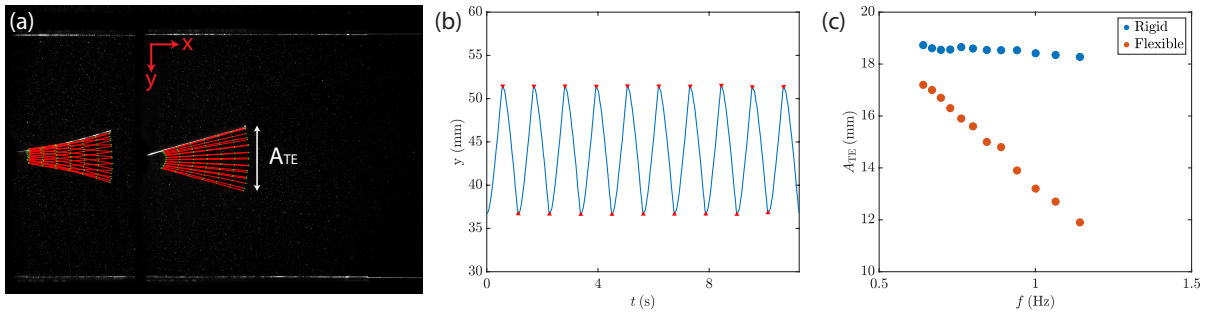


FIG. 6. **Dynamic motions extracted by tracking.** (a) Centerline (red) of the panel top view with solid post locations (green) marked on the flexible (left) and rigid (right) panel pitching at $f = 0.89$ Hz. (b) Example of TE motion tracking from the flexible panel pitching at $f = 0.89$ Hz. (c) Compiled A_{TE} as a function of f for both panels.

Hereafter, we consider the pitching panels. We first characterized the kinematics of the rigid and flexible panels by tracking their motion in the 2D top view. As shown in FIG. 6(a), the centerline of the panel (Red) was traced out from the DPIV masks and the locations of the solid posts (Green) separating the perforation holes were evenly distributed along the centerline according to the actual dimensions. The rigid panel sweeps out a true circular sector with negligible chord-wise deformation, while the flexible panel sweeps over a smaller funnel-shaped area due to bending. The TE positions were tracked using MATLAB

package DLTdv8 [73] and the subtraction between peaks and troughs defines the peak-to-peak amplitude (A_{TE}) (FIG. 6(b)). In summary, the rigid panel experiences little deformation across the tested f range, whereas the flexible panel undergoes more bending and smaller A_{TE} at higher f (FIG. 6(c)). For reference, kinematic conditions and St_A are summarized in Table I.

f (Hz)	Panel	A_{TE} (mm)	U_∞ (mm/s)	St_A
0.64	Rigid	18.7	17.0	0.647
	Flexible	17.2		0.706
0.67	Rigid	18.6	17.0	0.670
	Flexible	17.0		0.733
0.70	Rigid	18.5	17.0	0.684
	Flexible	16.7		0.761
0.73	Rigid	18.6	17.0	0.699
	Flexible	16.3		0.794
0.76	Rigid	18.7	17.0	0.713
	Flexible	15.9		0.837
0.80	Rigid	18.6	17.0	0.732
	Flexible	15.6		0.876
0.84	Rigid	18.5	17.0	0.745
	Flexible	15.0		0.921
0.89	Rigid	18.5	17.0	0.775
	Flexible	14.8		0.971
0.94	Rigid	18.5	17.0	0.769
	Flexible	13.9		1.026
1.00	Rigid	18.4	17.0	0.780
	Flexible	13.2		1.084
1.06	Rigid	18.3	17.0	0.798
	Flexible	12.7		1.149
1.14	Rigid	18.3	17.0	0.797
	Flexible	11.9		1.228

TABLE I. Summary of the kinematics and St_A .

C. Vortex structure transitions

Pitching panels are known to shed different vortex structures into the wake region depending on the oscillation frequency, amplitude, and the oncoming flow speed, namely St_A . The phase diagrams for wake structure transitions of pitching non-perforated rigid hydrofoils in 2D has been documented [54]. However, little has been described for perforated flexible hydrofoils, hence our effort to examine the vortical structures and the transitions as a function of f in our system.

Across the tested f range, the rigid panel did not exhibit a drastic change in the vortex shedding mode. A 2P wake was consistent throughout all cases, meaning that every pitching cycle generated 2 pairs of counter-

rotating vortices (FIG. 7). Specifically, during each stroke, a large primary vortex and a small secondary vortex were created at the TE. The large primary vortex pairs with the small secondary vortex from the previous stroke. The smaller secondary vortex pairs with the large primary vortex from the next stroke. The relative position of the counter-rotating vortices in each pair always puts the large primary vortex closer to the center of the wake and the small secondary vortex on the outside. Each pair tends to squeeze a jet in the opposite direction to the oncoming background flow, leading to a reduced x velocity, u , along the bounding regions of the wake (FIG. 8). The secondary vortex is weaker in strength and smaller in size than the primary vortex, thus dissipating more quickly. At $f = 0.64$ Hz (FIG. 7(a)), the vortex pair has significant time to advect downstream before the creation of the next pair. This reduces the vortex dissipation and annihilation. As a result, vortices stay coherent for a long period of time and gets shed in the streamwise direction. The wake has no bounding shear layers on the side. The decent spatial separation between vortex pairs acts like an entrance that allows the fluid outside the wake to be entrained into the wake for potentially more thermal mixing. At $f = 0.89$ Hz (FIG. 7(b)), the same effects become less pronounced. The lateral fluid entrainment entrance becomes smaller due to the closer spacing between vortex pairs. The outer secondary vortex starts to evolve into a shear layer as it advects downstream. At $f = 1.14$ Hz (FIG. 7(c)), the outer secondary vortex quickly stretches and diffuses into a continuous shear layer due to the advection by the mean flow, rather than staying as a coherent structure. The formation of the bounding shear layers prohibits lateral entrainment and mixing. The inner primary vortex also disappears more quickly due to strong interactions and annihilation with the previous pitching cycle, resulting in little u increment in the wake center except for a small region close to the TE (FIG. 8(c)).

Conversely, pitching the flexible panel across the tested f range had drastic changes in the vortex shedding mode. As f increase from 0.64 Hz to 1.14 Hz, the vortex structure transitions from a non-bifurcating 2P wake to a 2P+2S wake and then to a bifurcating 2P wake. Due to the flexible material, the panel deflects into a more hydrodynamically favorable shape during the stroke reversal and allows water to flow more easily in the lateral direction at the TE. Another way to conceptually understand this difference is the Kutta condition: the flow cannot realistically wrap around a sharp TE and thus has to exit the TE smoothly. The flexible panel's bending at the stroke reversal increases the slope of the curvature near the TE, making it point more laterally than the rigid panel. This leads to a stronger lateral component of the fluid velocity vector and a wider wake region than that behind the rigid panel. At $f = 0.64$ Hz (FIG. 9(a)), a non-bifurcating 2P wake occurs. Every stroke, a long golf-club-shaped vortex is created at the TE. There is a strong concentrated vortex core first generated during the initial sweep of the stroke and followed by a slender vortex sheet that stays connected between the vortex core and the TE. They are shed together after the stroke recovery to be advected downstream while being stretched even more laterally. Eventually, they sever into

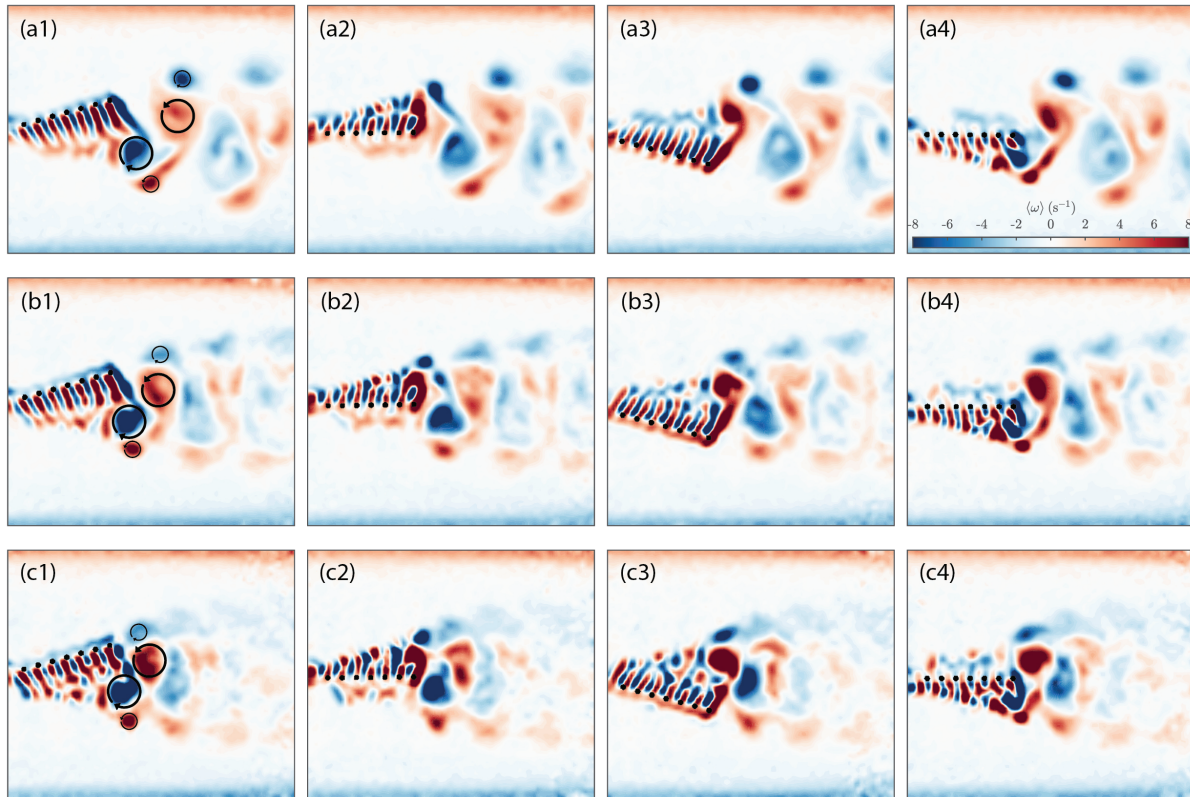


FIG. 7. **Wake vortex structure transition illustrated by phase-averaged snapshots from DPIV with the rigid panel.** (a) A coherent 2P wake at $f = 0.64$ Hz, similar to the flexible panel at the same f . (b) A similar 2P wake at $f = 0.89$ Hz, with the vortex pair separation reduced. (c) A very localized 2P wake at $f = 1.14$ Hz, with very small vortex pair separation leading to continuous shear layers bounding the wake. (1-4) Numbers correspond to 0, 25, 50, 75% progress of a phase-averaged cycle. **Note:** Red is counter-clockwise; Blue is clockwise. $\langle \omega \rangle$ denotes the phase-averaged vorticity.

two distinct vortices to contribute to different vortex pairs. Specifically, the leading vortex pairs up with the secondary vortex from the previous stroke, and the secondary vortex pairs up with the leading vortex of the following stroke. One may observe the high vortex structure similarity between the $f = 0.64$ Hz cases with flexible and rigid panels (FIG. 7(a) & 9(a)). This is understandable since the amount of chord-wise bending reduces with lower f . Thus, the kinematics and shapes of both flexible and rigid panels at this f are similar (FIG. 6(c)), resulting in overall similar flow patterns (FIG. 8(a) & 10(a)). At $f = 0.89$ Hz (FIG. 9(b)), a 2P+2S wake occurs due to the further severing of the TE vortex sheet. During every stroke, the long TE vortex splits into three relatively equal strength and spacing vortex cores. The two vortex cores on the side pair up with those from the previous and the next strokes. The vortex core in the middle sheds along the centerline alone as a single vortex. The vortex pair orients the jet in a direction that opposes the background mean flow, effectively slowing down u along the outer regions of the wake (FIG. 10(b)). The single vortices along the centerline interact with the vortex pairs on the side to generate more oscillatory

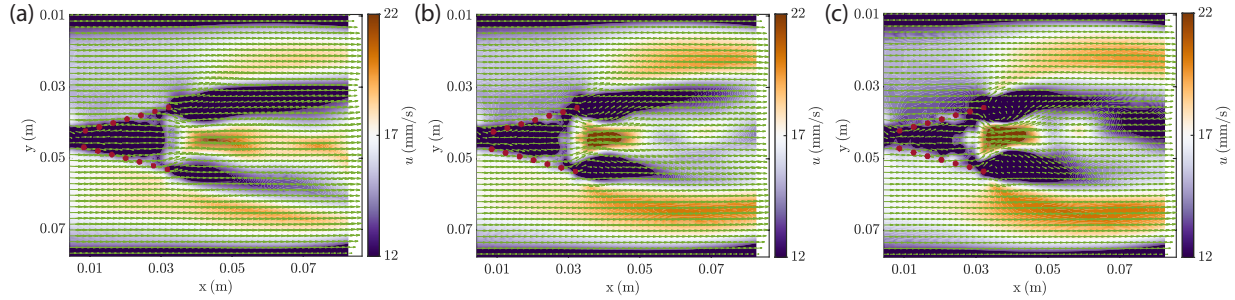


FIG. 8. **Time-averaged velocity field showing the mean flow behavior contributing to the fluid convection in the wake of the rigid panel.** (a) $f = 0.64$ Hz, (b) $f = 0.89$ Hz, and (c) $f = 1.14$ Hz. Red dots outline the sweeping range.

mean u profiles in the central wake region (FIG. 10(b)). At $f = 1.00$ Hz (FIG. 9(c)), a bifurcating 2P wake diverges from the centerline of the pitching motion. The orientation of the vortex pair changes such that the jet has a slightly opposing angle initially and rotates to a neutral or slightly favorable angle with respect to the oncoming u later downstream. Intuitively, the time-averaged velocity shows mild u decrease close to the maximum positions of TE and mild increment along two bifurcating jets later downstream. Between the bifurcating jets is a small uniform convection zone with reduced u (FIG. 10(c)). At $f = 1.14$ Hz (FIG. 9(d)), the similar bifurcating 2P wake occurs. The orientation of the vortex pair directs the jet at a favorable angle which accelerates the oncoming u . Between the laterally parting vortex pairs, water moves slowly with weaker periodicity. Combined, the time-averaged velocity field has laterally bifurcating jets of increased u and a central region with reduced u for steady uniform thermal convection (FIG. 10(d)). Despite the minor differences, $f = 1.00$ and 1.14 Hz share the same vortex breakup mechanism. During every stroke, a TE vortex keeps accumulating circulation and stretches across the entire A_{TE} . Close to the end of the stroke, this long vortex sheet severs into two, one weaker and one stronger. The weaker vortex pairs up with the stronger vortex from the previous stroke and gets shed. The stronger vortex lingers and pairs up with the weaker vortex from the next stroke. This 2P mechanism is fundamentally different from the 2P wake behind an oscillating non-perforated rigid foil reported by Schnipper *et al.* [54]. In their case, the 2P wake is created due to the time difference between the TE vortex creation and the LE vortex rolling across the entire chord. Thus, their vortex pair is consisted of one TE vortex and one LE vortex. However, in our case, the perforation prevents the roll and growth of the LE vortex due to the absence of the traditionally defined velocity boundary layer. Thus, both vortices in a pair come from the TE motion.

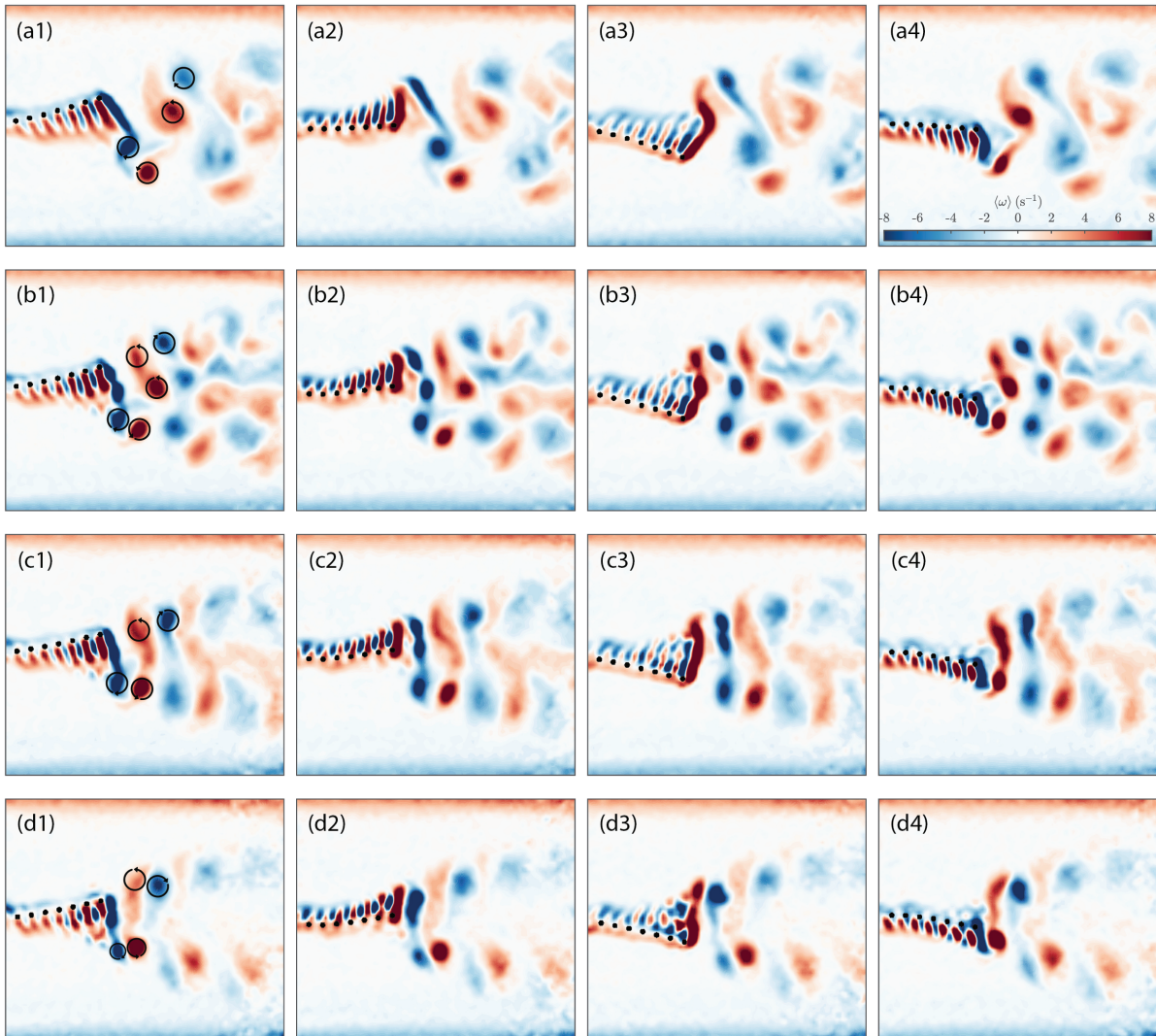


FIG. 9. Wake vortex structure transition illustrated by phase-averaged snapshots from DPIV with the flexible panel. (a) A non-bifurcating 2P wake at $f = 0.64$ Hz with an orientation opposing the mean flow, similar to the rigid panel at the same f . (b) A 2P+2S wake at $f = 0.89$ Hz creating oscillating flow profiles across the width of the wake. (c) A bifurcating 2P wake at $f = 1.00$ Hz with the orientation transitioning from slightly opposing to slightly accelerating the mean flow. (d) A bifurcating 2P wake at $f = 1.14$ Hz with an orientation accelerating the mean flow. (1-4) Numbers correspond to 0, 25, 50, 75% progress of a phase-averaged cycle. **Note:** Red is counter-clockwise; Blue is clockwise. $\langle \omega \rangle$ denotes the phase-averaged vorticity.

D. Lagrangian coherent structures

Lagrangian coherent structures (LCS) have been widely used to understand the fluid mixing in ocean engineering [74], turbulence [75], and biological flows [76, 77]. Specifically, the hyperbolic LCS outlines the boundaries of the fluid pockets that undergo translation, rotation, and deformation over time. The Finite-Time Lyapunov Exponent (FTLE) is used to quantitatively illustrate the stable and unstable manifolds that

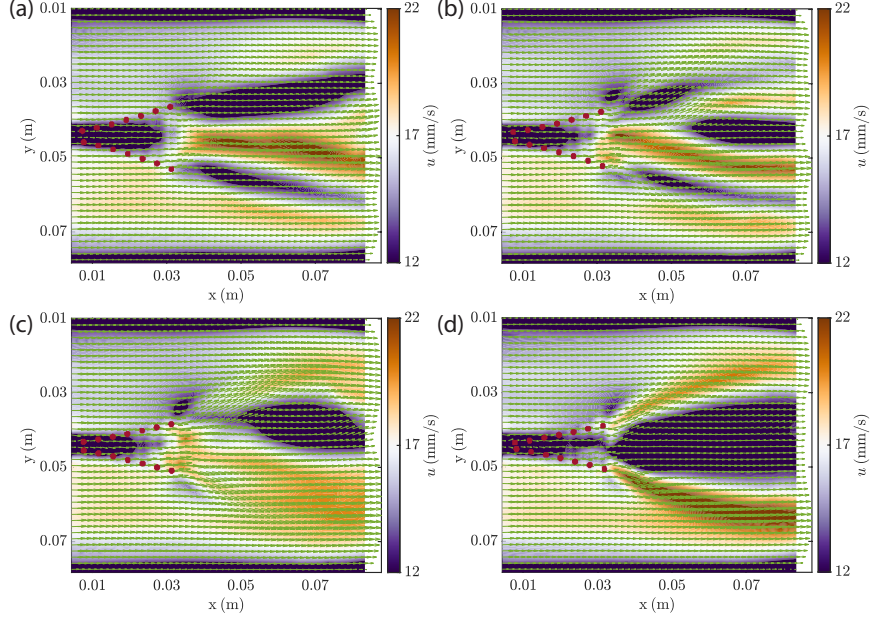


FIG. 10. **Time-averaged velocity field showing the mean flow behavior contributing to the fluid convection in the wake of the flexible panel.** (a) $f = 0.64$ Hz, (b) $f = 0.89$ Hz, (c) $f = 1.00$ Hz, and (d) $f = 1.14$ Hz. Red dots outline the sweeping range.

physically correspond to fluid element contraction and stretching along the LCS respectively [78]. The contracting and stretching of fluid elements in different directions creates saddle points that function as the expressway intersections for material transport and mixing. The mathematical theory for computing FTLE has been detailed in the pioneering works by Shadden, Haller, and Brunton, et al. [79–81]

We borrow the MATLAB package developed by Dabiri *et al.* for computing the hyperbolic LCS. Foundations, validations, and applications of this package can be found in published works [76, 82]. Essentially, a matrix of equally-spacing particle flow map (our case: 194×168 particles) is initialized in the fluid velocity field obtained from the experiment (our case: phase-averaged velocity) and allowed to transport freely with the flow by an integration over forward- or backward-time. Across each time step from t to $t + \delta t$, the flow map Jacobian \mathbf{J} for each particle can be approximated as

$$\mathbf{J} = \begin{bmatrix} \frac{\partial x(t_0 + \delta t)}{\partial x(t_0)} & \frac{\partial x(t_0 + \delta t)}{\partial y(t_0)} \\ \frac{\partial y(t_0 + \delta t)}{\partial x(t_0)} & \frac{\partial y(t_0 + \delta t)}{\partial y(t_0)} \end{bmatrix}. \quad (6)$$

The Cauchy-Green strain tensor (Δ) is equal to the multiplication of \mathbf{J} with its own transpose \mathbf{J}^T . The eigenvector and the eigenvalue of Δ represent the direction and the amount of maximum stretching of the specific fluid element in forward- or backward-time depending on the integration. Then the FTLE can be calculated as

$$\text{FTLE} = \frac{1}{|\delta t|} \log \left(\sqrt{\lambda_{\max}(\mathbf{\Delta})} \right) . \quad (7)$$

where λ_{\max} is the maximum eigenvalue of the matrix $\mathbf{\Delta}$. The FTLE from forward- or backward-time integration can be denoted as pFTLE or nFTLE respectively.

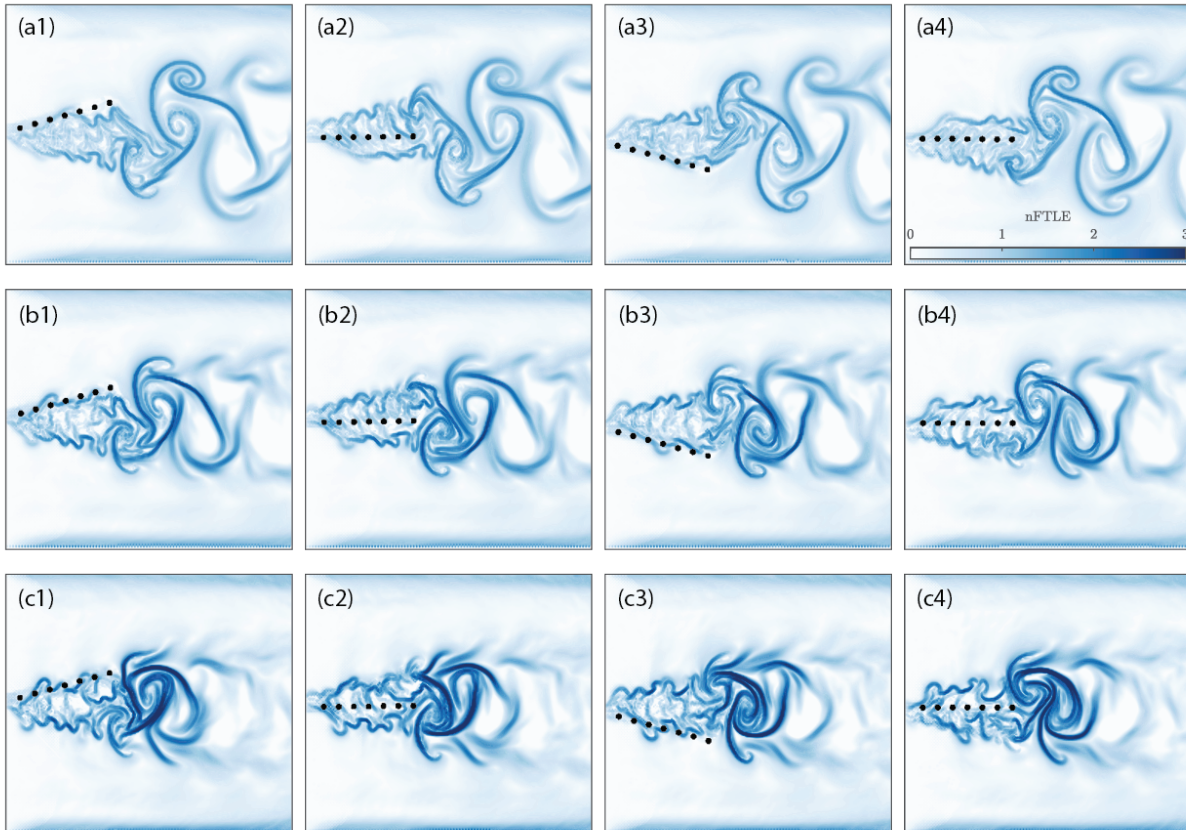


FIG. 11. **Attractive LCS illustrated by nFTLE around the rigid panel.** (a) $f = 0.64$ Hz, (b) $f = 0.89$ Hz, (c) $f = 1.14$ Hz, (1-4) Numbers correspond to 0, 25, 50, 75% progress of a phase-averaged cycle.

In this work, we only compute and examine the nFTLE by integrating backward in t for one stroke cycle. High nFTLE values form ridges that represent the unstable manifolds which express the flow structure stability since fluid elements are attracted to them, hence the other name “attractive LCS”. Previous works have shown its ability to trace the movement of fluid tracers (chemical [83] and inertial particles [77]) in the flow, analogous to the thermal convection of hot water blobs. The hot water zone near the pitching panel can be thought as the fluid tracer. It will be attracted to the nFTLE ridges and stretched along these ridges to be mixed in the vortex wake. The shape of the hot water blobs will conform to the shape of the nFTLE ridges without much area change due to the incompressible approximation and 2D assumption. Therefore, the

nFTLE ridges represent where the hot water will go. The shape of the nFTLE ridges shows us how the hot water blob will be stretched and whether it will fold onto itself [80]. The distribution of the nFTLE field will tell us whether the hot water is stretched evenly across the domain or staying local. A wider distribution of higher nFTLE values means the hot water blob will be spread more quickly and widely, which encourages thermal convection and mixing.

As shown in FIG. 11 & 12, the ridges highlight the LCS in the wake to be consistent with the boundaries of the vortices shown in FIG. 7 & 9. On the superficial level, the nFTLE ridges confirm the identified vortex structure transitions from non-bifurcating 2P to 2P+2S then to bifurcating 2P with the flexible panel. On the fluid mixing perspective, the ridges function as an invisible boundary for fluid motion, meaning that fluid elements should remain on either side of the ridge without crossing over [78, 83]. This helps determine which fluid region comes from the hot zone swept by the perforated panel and which is entrained from the cold background flow on the side.

For the rigid panel, at $f = 0.64$ Hz (FIG. 11(a)), the 2P wake sheds coherently along the centerline downstream, and there's enough separation between adjacent LCS to entrain cold water into the hotter wake to enhance mixing. As f increases to 0.89 and 1.14 Hz (FIG. 11(b-c)), the nFTLE ridges are highly compacted right behind the TE with relatively high values. This represents a strong stretching and folding of the hot water limited to this localized area without much persistence into the farther regions. The continuous bounding shear layers mentioned before for $f = 1.14$ Hz also match the nFTLE ridges on the side that provide nearly no entrance for cold water entrainment. From this trend, we anticipate that pitching the rigid panel at a higher frequency would negatively influence thermal mixing in the wake.

For the flexible panel, at $f = 0.64$ Hz and $f = 0.89$ Hz (FIG. 12(a-b)), large flow entrainment entrances exist which allow the lateral thermal mixing between the hot and cool water to happen more aggressively in the wake region. Note the LCSs for both panels are very similar at $f = 0.64$ Hz, as discussed already in Section IV.C. As f increases to 1.00 and 1.14 Hz (FIG. 12(c-d)), the laterally growing LCS (mushroom-shaped pockets corresponding to the vortex pairs) from different stroke cycles are relatively close to each other, making the nFTLE ridges compacted. This leaves the entrance for lateral flow entrainment to be relatively smaller, although still much larger than the rigid panel at the same frequencies. Therefore, we anticipate the thermal mixing performance to be overall better with the flexible panel than the rigid panel.

Statistical analysis can be done on the nFTLE in the wake region beyond the panel ($x > 0.035$ m) to quantify the stretching distribution and anticipate different thermal mixing performances. Probability density functions (PDF) of the mean nFTLE field over one stroke cycle help us visualize the distribution of fluid stretching in the region of interest. As shown in FIG. 13, the flexible panel generally has a higher nFTLE contribution in the ranges of $0.5 \sim 0.8$ (FIG. 13(a)), $0.5 \sim 1.2$ (FIG. 13(b)), and $0.5 \sim 1.5$

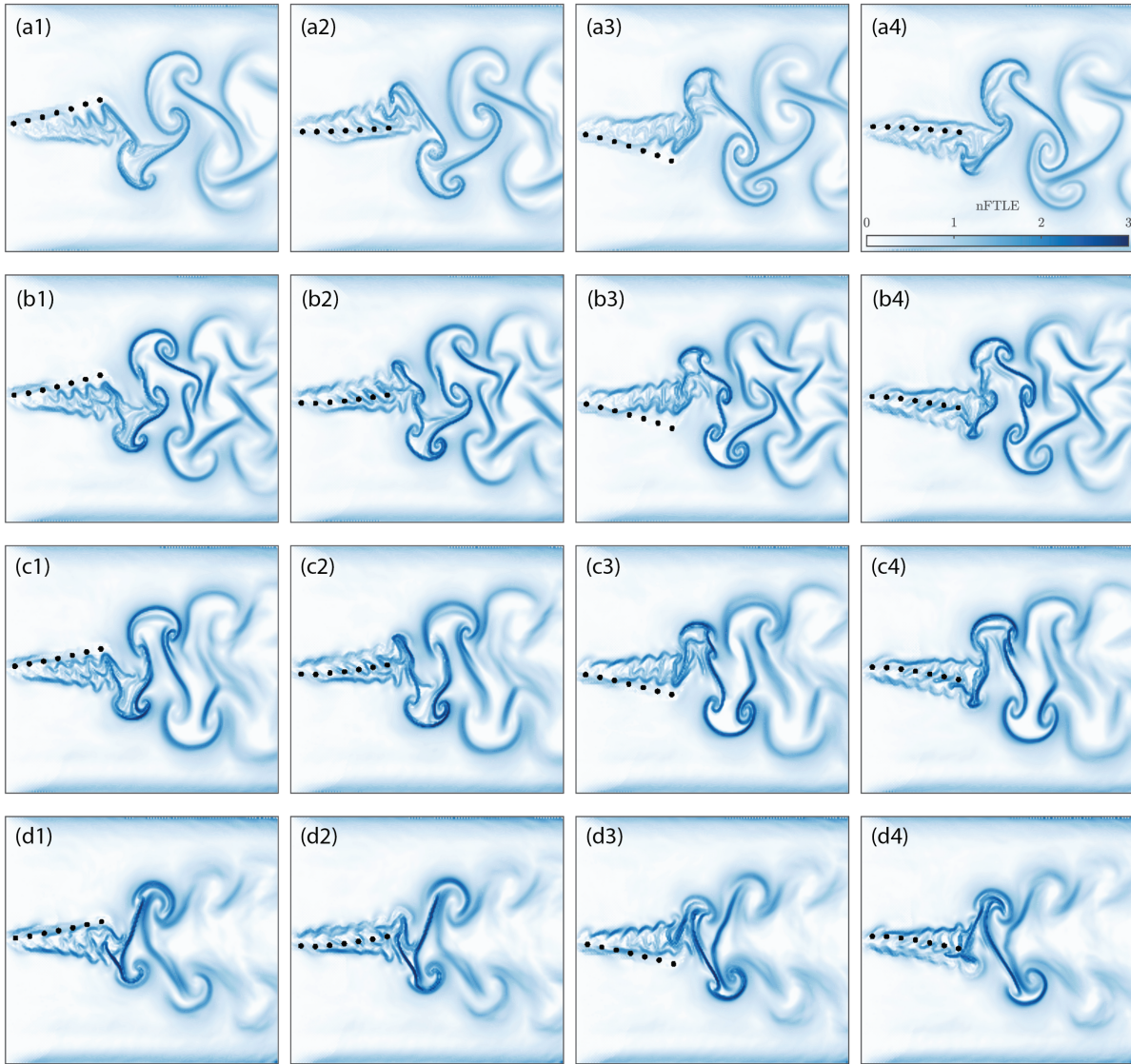


FIG. 12. **Attractive LCS illustrated by nFTLE around the flexible panel.** (a) $f = 0.64$ Hz, (b) $f = 0.89$ Hz, (c) $f = 1.00$ Hz, (d) $f = 1.14$ Hz, (1-4) Numbers correspond to 0, 25, 50, 75% progress of a phase-averaged cycle.

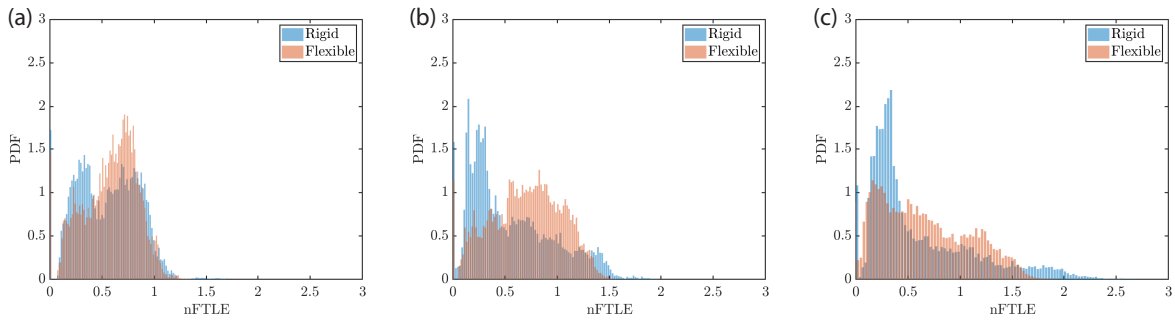


FIG. 13. **Probability density function (PDF) of the time-averaged nFTLE over one stroke cycle in the wake region.** Comparisons were done between rigid and flexible panels for three representative pitching frequencies, (a) $f = 0.64$ Hz, (b) $f = 0.89$ Hz, and (c) $f = 1.14$ Hz.

(FIG. 13(c)). This indicates that the flexible panel's motion creates stronger fluid stretching of the hot water blob in a wider region in the wake, which is helpful for dispensing the heat in a larger range. One can notice that at $f = 0.89$ and 1.14 Hz, the rigid panel has a longer right-skewed tail with high nFTLE values that are absent for the flexible panel. This is in consistency with the nFTLE contours showing that the rigid panel can induce stronger fluid stretching than the flexible panel, but only in a very localized fashion. The right-skewed high nFTLE values indeed lead to some chaotic mixing [84] and enhance the thermal mixing near the TE, but does not translate to the overall mixing effect. To further quantify the nFTLE distribution, we compute the skewness (γ), sum, mean, and standard deviation within the wake region. Regarding skewness, homogeneous and heterogeneous mixing have been defined to separate the cases of global uniform mixing and strong localized mixing [85, 86]. For homogeneous mixing, the nFTLE distribution is expected to follow a Gaussian distribution ($\gamma = 0$), while heterogeneous mixing's would be highly skewed. Empirically, a skewness value $\gamma \in [-0.5, 0.5]$ can be classified as approximately symmetric, in other words more homogeneous mixing. The flexible panel fell within the symmetric threshold for all tested f , whereas the rigid panel fell in the symmetric threshold only at $f \in [0.64, 0.73]$ Hz (FIG. 14(a)). Specifically, the rigid panel continues to become more skewed with an increasing f , whereas the flexible panel has less skewness for an intermediate f range. However, we refrain from making further claims due to γ 's sensitivity to experimental values. We argue that the distinction between inside and outside the symmetric threshold has more practical implications on mixing. We also found that the flexible panel yields a generally higher sum and mean of nFTLE in the wake region, indicating its better thermal mixing ability (FIG. 14(b-c)).

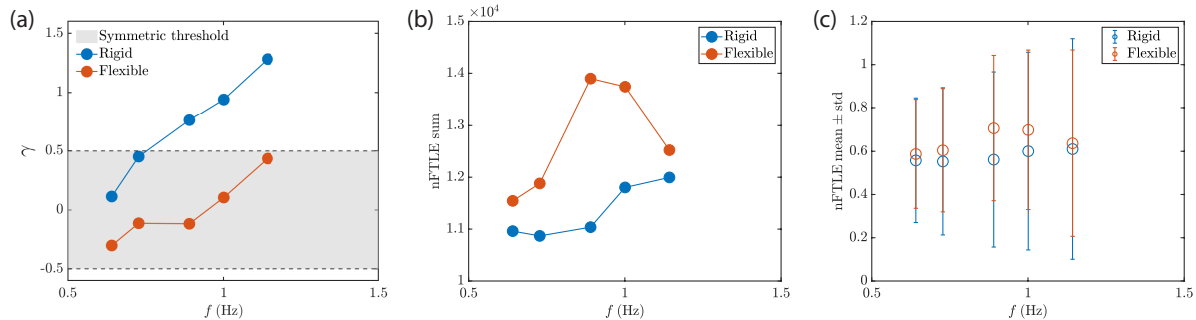


FIG. 14. **Statistical analysis of the nFTLE field.** (a) Skewness of the nFTLE distributions in the region of interest ($x > 0.035$ m) at $f = 0.64, 0.73, 0.89, 1.00,$ and 1.14 Hz. (b) Sum of the nFTLE values representing total fluid stretching in the same cases. (c) Mean and standard deviation of the nFTLE values representing the spread of fluid stretching in the same cases.

E. Thermal mixing of the temperature field

Finally, we examine the simulated temperature field to consolidate the understandings from the previous analysis. Since the uniform background inflow is assumed to have a constantly low temperature source and all heating comes from the solid posts separating the perforation holes on the panel, the mixing performance should be characterized by the spread of T in the domain. As expected, the high temperature fluid pockets leave the thermal boundary layer next to the panel and gets transported into the wake with stretching and cold fluid entrainment paths outlined by the nFTLE ridges around the vortex boundaries (FIG. 15 & 16). This is consistent with the definition of attractive LCS as fluid boundaries and unstable manifolds.

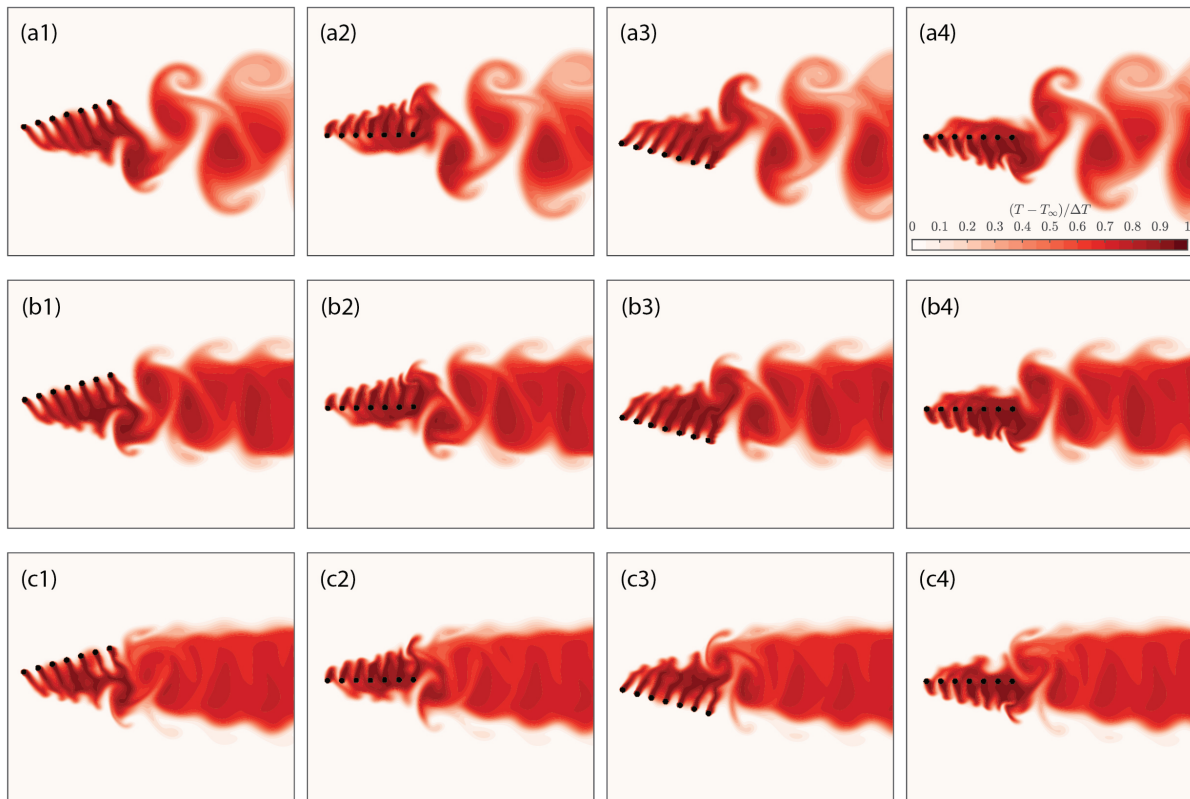


FIG. 15. **Temperature fields during the 11th stroke cycle of the rigid panel.** (a) $f = 0.64$ Hz, (b) $f = 0.89$ Hz, (c) $f = 1.14$ Hz, (1-4) Numbers correspond to 0, 25, 50, 75% progress of a phase-averaged cycle.

Comparing the T_{mean} evolution with time (FIG. 17(a)) and the \bar{T} across the last 5 pitching cycles (FIG. 17(b)) from the simulation, both rigid and flexible panels performed better than the static case [Section IV.I], proving that the prescribed motion is effectively enhancing the thermal performance. Counterintuitively, the rigid panel reaches a higher \bar{T} than the flexible panel in all cases. This is likely from the effect of a short-lived and localized LCS in the wake, which does not contribute to streamwise convection of heat as much

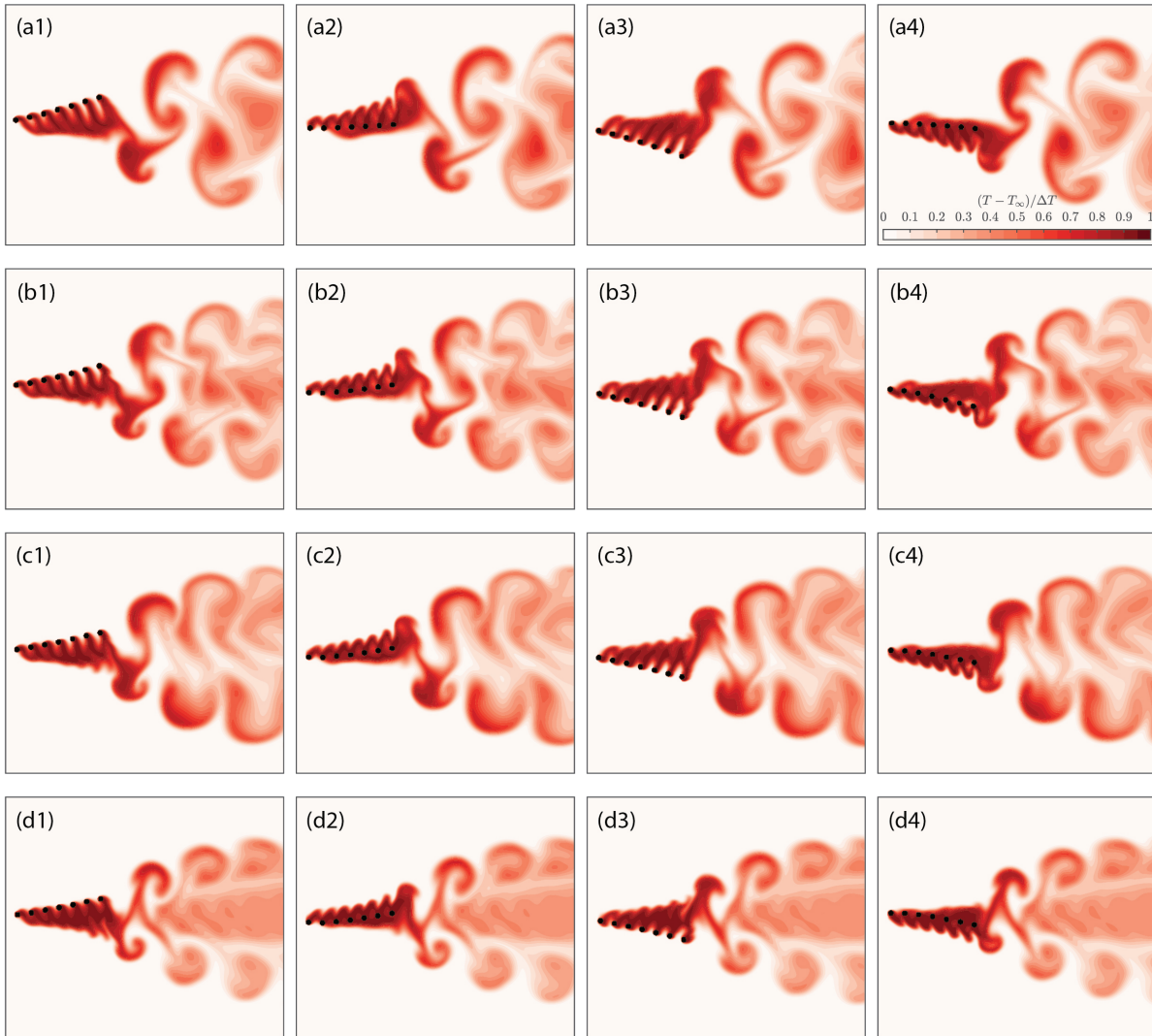


FIG. 16. **Temperature fields during the 11th stroke cycle of the flexible panel.** (a) $f = 0.64$ Hz, (b) $f = 0.89$ Hz, (c) $f = 1.00$ Hz, (d) $f = 1.14$ Hz, (1-4) Numbers correspond to 0, 25, 50, 75% progress of a phase-averaged cycle.

as the flexible panel wake (compare FIG. 8 & 10). The shear layer blockage of the lateral entrainment also adds to the excessive heating in the rigid panel wake. If the purpose is to elevate the \bar{T} of the domain, the rigid panel may be a better option than using flexible material. However, \bar{T} alone does not represent the thermal mixing capability, which could be more important for certain applications where a more uniform downstream temperature distribution is needed. The thermal wake width to TE amplitude ratio (W/A_{TE}) reflects the panel's ability to transfer heat in the transverse direction. Results in FIG. 17(c-d) shows that the flexible panel is indeed more capable of distributing heat in a wider thermal wake. The true W of the flexible panel stays relatively constant with increasing f , but the deflection keeps decreasing the A_{TE} , which leads to an increasing W/A_{TE} . This means for the same flexible panel, pitching at a higher f is able to maintain

the same level of lateral thermal dispersion with a smaller lateral movement. Since A_{TE} remains a constant for the rigid panel, the W/A_{TE} trend reflects the true W . As f increases, a shrinkage of the thermal wake width is noticed for 0.64 - 0.76 Hz, then followed by a plateau at higher f . This indicates that the rigid panel's capability to transfer heat laterally in the wake does not benefit from faster pitching, opposite from the flexible panel. Another metric to evaluate thermal mixing is the equilibrium outlet mixing index (MI), defined as

$$MI = \frac{1}{\Delta t} \int_{t_0}^{t_0+\Delta t} \left(1 - \frac{1}{T_{\text{outlet}}^{\text{mean}}(t)} \sqrt{\frac{\sum_{i=1}^n [T(y_i, t) - T_{\text{outlet}}^{\text{mean}}(t)]^2}{n}} \right) dt, \quad (8)$$

following the work of Lambert and Rangel [87], where Δt (5 cycles) is the time-averaging window size, $T(y_i, t)$ is the local temperature value at various y locations along the outlet column, $T_{\text{outlet}}^{\text{mean}}$ is the mean temperature across the outlet column, and n is the number of data points in the outlet column. MI is by definition a value between 0 (no mixing) and 1 (fully mixed). As shown in FIG. 17(e), the flexible panel achieved overall better mixing at the outlet than the rigid panel. As mentioned before, the flexible panel's thermal wake width W does not change significantly as a function of f , and thus the outlet MI stays relatively constant across all f . However, the rigid panel did show a W shrinkage with increasing f in the lower range, which is reflected as the decreasing MI for the same range. Note that faster pitching is compensated by potentially more power input due to the faster solid object motion and higher hydrodynamic power. Quantification of the power input requires a deeper understanding of the flexural rigidity, hydrodynamic forcing, and added mass effect of such perforated panels. Since the current focus is on the vortex transition and thermal mixing, we leave efficiency evaluation for future exploration.

Similar to the nFTLE field, we also examine the probability density function of the wake T field ($x > 0.035$ m) averaged over the last five cycles to distinguish the performances between rigid and flexible panels. Overall, the rigid panel yielded more higher temperature concentrations in the field than the flexible panel, also shown in FIG. 17(a-b). At low f , the rigid panel benefits from the vortex structure transition and the periodic breaking of the bounding shear layer, hence the resulting T distribution in FIG. 18(a). At higher f , the rigid panel results in one spike at 300 K, one spike at around 335 - 340 K, and nearly nothing in between (FIG. 18(b-c)). This indicates low thermal mixing due to the sharp delineation between the interior and exterior sides of the wake. The non-mixing wake separates the resulting temperature field into an almost uniformly heated wake and non-heated external flow (heterogeneous thermal mixing). On the other hand, the flexible panel across all f resulted in better thermal mixing. A wider distribution in the intermediate T range demonstrate the more uniform distribution of heat throughout the flow field (homogeneous thermal

mixing).

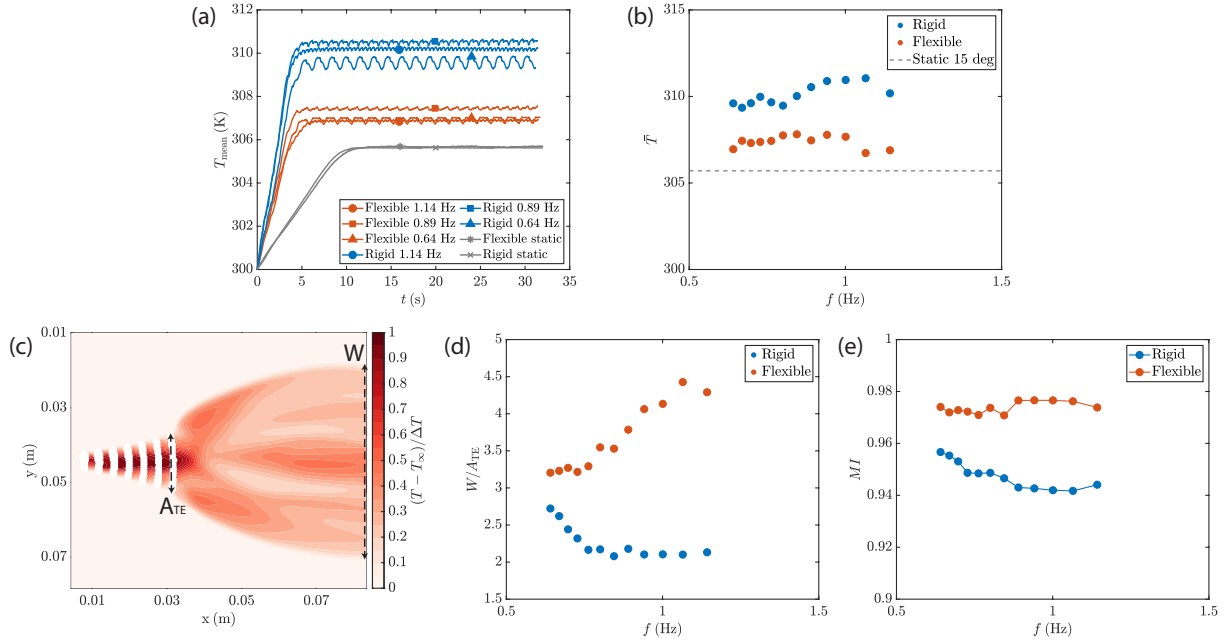


FIG. 17. **Equilibrium temperature field over the last 5 pitching cycles of the simulation.** (a) Domain-averaged temperature evolution over time from example cases. (b) Equilibrium temperatures for all tested conditions. (c) Definition of the thermal wake width. (d) Normalized thermal wake width as a function of f . (e) Mixing index at the right outlet.

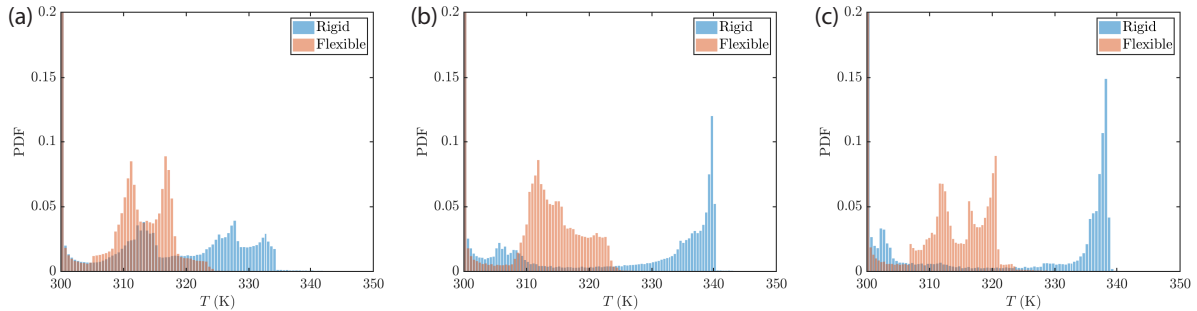


FIG. 18. **Temperature contributions in the time-averaged field over the last 5 pitching cycles in the simulation for the wake region beyond the panel ($x > 0.035$ m).** Comparisons quantify the different thermal mixing and temperature distributions between the rigid and flexible panels at (a) $f = 0.64$ Hz, (b) $f = 0.89$ Hz, and (c) $f = 1.14$ Hz.

V. CONCLUSION AND DISCUSSION

Our work provides the first characterization of actively pitching perforated panels regarding the vortex structure transition, Lagrangian coherent structures, and thermal mixing. Comparisons were made between

panels with different chord-wise flexibilities and pitching frequencies. Our results demonstrated that the thermal mixing benefits greatly from the prescribed motion due to the creation of unsteady wake vortex streets. Panels with pitching motion, regardless of the chord-wise flexibility and pitching frequency, all reached a higher domain-averaged equilibrium temperature than the static scenario by an approximately 30% - 78% margin (FIG. 17(a-b)). The panel without chord-wise flexibility does not experience a fundamental vortex structure change within the tested f range. Lateral entrainment and the associated thermal mixing between the hotter wake flow and the colder incoming flow depend on the periodic breaking of the bounding shear layers which becomes prominent only at lower frequency ranges. Due to local vortex annihilation, thermal convection is suppressed in the wake, resulting in a sharper temperature gradient across the bounding shear layers. The panel with chord-wise flexibility, however, experiences fundamentally different vortex structure modes when pitched at different f . Specifically, a transition from non-bifurcating 2P to 2P+2S then to bifurcating 2P is documented along with increasing frequency. The perforation invokes a different vortex shedding mechanism than those described on non-perforated hydrofoils [54]. Both LCS and simulated temperature showed that chord-wise flexibility enhances lateral thermal mixing entrainment and more-homogeneous mixing. Our work innovatively explores the FSI of actuated flexible panels with porosity, a topic that is very much neglected in the literature and underestimated for its application. We drew new connections between unsteady hydrodynamics of vortex shedding and heat-mass transfer. Our work not only extends the fundamental understanding of flexible vortex generators but also provides insights for novel biomimetic designs of thermal and material dispensing systems. Several directions for future work are discussed below.

A. Simulation boundary conditions

In order to study the vortex generation and thermal mixing, the current Convection Diffusion simulation adopts a simplified boundary condition on both the fluid and the solid domain. The moving solid structure is isothermal at 350 K. When the solid structure moves to the new location in the next frame, the ghost cells in the fluid domain (the nodes previously occupied by solid) are assumed to be heated up to 350 K as the initial condition for the next time segment's simulation [Details explained in Section III.B.]. This essentially assumes that we have an ultra-effective heat source that allows infinitely fast thermal conduction of heat from the hotter solid to the surrounding fluid. In reality, the amount of conductive heating would depend on the temperature gradient, thermal conductivity, and time, making it possible for the ghost cell fluid elements to start at a temperature lower than the solid's. The same issue applies to the material transport problems as the cross-membrane filtration depends on the concentration gradient, diffusion coefficient, membrane porosity,

and time. Currently, we make sense of our assumptions due to the fine temporal discretizations from the high-speed video and the ODE45 auto-stepping: large overlapping of the moving solid structure exists in two adjacent frames. The Neumann constant flux boundary condition at the flow outlet may also introduce error. Though common in similar channel flow simulations [27, 71, 88], the horizontal domain size may be too small to assume complete stabilization of the flow and temperature in the streamwise direction, owing to the periodic wake. For now, we are comfortable with our simulation results since the solver validations match published data. However, we acknowledge the limitations of this current simulation method. More realistic settings of the boundary conditions (such like isothermal, isoflux, and more complicated cases depending on the physical properties) and iterative time stepping schemes might improve the simulation to reflect more application-relevant engineering situations. Such improvement will enable us to study local transport phenomenon near the perforations including saturation and fatigue [36].

B. Complex actuation

Other kinematics and flexural rigidities are worth investigation too. As discussed by Quinn *et al.* [89], flexible panels' deformation in fluid can be modelled by the Euler-Bernoulli Beam Theory, which predicts different modes of resonance frequencies. As a function of the kinematic boundary condition (sinusoidal pitching, heaving, flapping, temporal asymmetry, and spatial asymmetry) and the flexural rigidity, these resonance modes may play a role in the vortex formation and thermal mixing, as they do to hydrodynamic force production [89, 90]. We conducted preliminary experiments with LE pitching at even higher frequencies (~ 3 Hz). The flexible panel sustains more deformation, similar to the second resonance. The panel, though slender and perforated, acts like a bluff body and creates a non-shedding circulating wake like those observed by Shang *et al.* [91]. This wake has an oscillation frequency much slower than the pitching f , making it trickier for the simulation pre-processing. Due to the lack of strong vortex-induced mixing, we believe that they do not have better thermal mixing efficacy. Yet, explaining the FSI could contribute to the overall understanding of actuated perforated panels.

C. Implications to ichthyology and biomimetic engineering

Echoing with the biological inspiration from fish gill filaments, we believe future extensions from the present work may shed lights on the evolutionary optimization of this respiratory organ. Fish gills are subject to different incoming flow conditions: continuous for ram ventilation and pulsatile for opercular pumping [34]. Fish gills also operate at a wide range of Re , making the optimal pore size important for

gas exchange [92]. Furthermore, fish have multiple gill sets in parallel, potentially harvesting benefits from the inter-lamellar interactions. All these details can be translated to similar engineering problems, so the exploration potential is vast.

VI. ACKNOWLEDGEMENT

We are grateful for the discussions with Haibo Dong, Zihao Huang, and Daniel B. Quinn at the University of Virginia, and the Bio-inspired Fluid Lab at Cornell University. We thank Casey Dillman at Cornell University Museum of Vertebrates for providing fish gill samples. Y.F. acknowledges the funding support from Cornell University CALS Alumni Associate Award. Y.F. and S.J. acknowledge the partial funding support from the U.S. National Oceanic and Atmospheric Administration (NOAA-NA24OARX417C0598-T1-01) and the U.S. National Science Foundation (CMMI-2042740 & CBET-2401507).

VII. AUTHOR CONTRIBUTIONS

Y.F. conceived the idea; Y.F., S.T., and J.G. conducted experiments. Y.F. and Z.L. conducted simulations. Y.F., S.T., and J.G. analyzed data. S.J. supervised the research. Y.F., S.T., and J.G. wrote the original manuscript. Y.F., Z.L., S.T., J.G., and S.J. reviewed the manuscript.

VIII. CONFLICT OF INTERESTS

The authors declare no competing interests.

-
- [1] Tiezheng Tong and Menachem Elimelech, “The global rise of zero liquid discharge for wastewater management: drivers, technologies, and future directions,” *Environmental science & technology* **50**, 6846–6855 (2016).
- [2] Mangalore Vikas and GS Dwarakish, “Coastal pollution: a review,” *Aquatic procedia* **4**, 381–388 (2015).
- [3] Ali Habibi Khalaj and Saman K Halgamuge, “A review on efficient thermal management of air-and liquid-cooled data centers: From chip to the cooling system,” *Applied energy* **205**, 1165–1188 (2017).
- [4] DaWei Wu and RuZhu Wang, “Combined cooling, heating and power: A review,” *progress in energy and combustion science* **32**, 459–495 (2006).
- [5] Jonathan Himmelfarb, Raymond Vanholder, Rajnish Mehrotra, and Marcello Tonelli, “The current and future landscape of dialysis,” *Nature Reviews Nephrology* **16**, 573–585 (2020).
- [6] Chris M Wood and Junho Eom, “The osmorespiratory compromise in the fish gill,” *Comparative Biochemistry and Physiology Part A: Molecular & Integrative Physiology* **254**, 110895 (2021).
- [7] Nelika K Hughes, Catherine J Price, and Peter B Banks, “Predators are attracted to the olfactory signals of prey,” *PLoS One* **5**, e13114 (2010).
- [8] Brain D Wisenden, “Olfactory assessment of predation risk in the aquatic environment,” *Philosophical Transactions of the Royal Society of London. Series B: Biological Sciences* **355**, 1205–1208 (2000).
- [9] Gautam Reddy, Venkatesh N Murthy, and Massimo Vergassola, “Olfactory sensing and navigation in turbulent environments,” *Annual Review of Condensed Matter Physics* **13**, 191–213 (2022).
- [10] Denise Chen and Jeannette Haviland-Jones, “Human olfactory communication of emotion,” *Perceptual and motor skills* **91**, 771–781 (2000).
- [11] Leanne A Grieves, Marc Gilles, Innes C Cuthill, Tamás Székely, Elizabeth A MacDougall-Shackleton, and Barbara A Caspers, “Olfactory camouflage and communication in birds,” *Biological Reviews* **97**, 1193–1209 (2022).
- [12] Hassan Aref, “The development of chaotic advection,” *Physics of fluids* **14**, 1315–1325 (2002).
- [13] Hassan Aref, “Stirring by chaotic advection,” in *Hamiltonian Dynamical Systems* (CRC Press, 2020) pp. 725–745.
- [14] Paul E Dimotakis, “Turbulent mixing,” *Annu. Rev. Fluid Mech.* **37**, 329–356 (2005).
- [15] CP Caulfield, “Layering, instabilities, and mixing in turbulent stratified flows,” *Annual Review of Fluid Mechanics* **53**, 113–145 (2021).
- [16] Guohua Zhang, Jian Liu, Bengt Sundén, and Gongnan Xie, “Combined experimental and numerical studies on flow characteristic and heat transfer in ribbed channels with vortex generators of various types and arrangements,” *International Journal of Thermal Sciences* **167**, 107036 (2021).
- [17] Lei Luo, Fengbo Wen, Lei Wang, Bengt Sundén, and Songtao Wang, “Thermal enhancement by using grooves and ribs combined with delta-winglet vortex generator in a solar receiver heat exchanger,” *Applied energy* **183**, 1317–1332 (2016).

- [18] Pongjet Promvonge, Teerapat Chompookham, Sutapat Kwankaomeng, and Chinaruk Thianpong, “Enhanced heat transfer in a triangular ribbed channel with longitudinal vortex generators,” *Energy Conversion and Management* **51**, 1242–1249 (2010).
- [19] Juan He, Qinghua Deng, and Zhenping Feng, “Film cooling performance enhancement by upstream v-shaped protrusion/dimple vortex generator,” *International Journal of Heat and Mass Transfer* **180**, 121784 (2021).
- [20] Chi-Chuan Wang, Kuan-Yu Chen, Jane-Sunn Liaw, and Chih-Yung Tseng, “An experimental study of the air-side performance of fin-and-tube heat exchangers having plain, louver, and semi-dimple vortex generator configuration,” *International Journal of Heat and Mass Transfer* **80**, 281–287 (2015).
- [21] LH Tang, WX Chu, N Ahmed, and M Zeng, “A new configuration of winglet longitudinal vortex generator to enhance heat transfer in a rectangular channel,” *Applied Thermal Engineering* **104**, 74–84 (2016).
- [22] Wenbo Han, Wei Li, and Hongpeng Zhang, “Insight into mixing performance of bionic fractal baffle micromixers based on murray’s law,” *International Communications in Heat and Mass Transfer* **157**, 107843 (2024).
- [23] Wei Liao and Dalei Jing, “Experimental study on fluid mixing and pressure drop of mini-mixer with flexible vortex generator,” *International Communications in Heat and Mass Transfer* **142**, 106615 (2023).
- [24] XL Zhong, Sau Chung Fu, Ka Chung Chan, G Yang, HH Qiu, and Christopher YH Chao, “Experimental study on the thermal-hydraulic performance of a fluttering split flag in a channel flow,” *International Journal of Heat and Mass Transfer* **182**, 121945 (2022).
- [25] Xueling Liu, Yunkai Leng, and Jiansheng Wang, “The heat transfer enhancement with a flag-shaped flexible wing,” *International Journal of Heat and Mass Transfer* **224**, 125362 (2024).
- [26] Jae Bok Lee, Sung Goon Park, Boyoung Kim, Jaeha Ryu, and Hyung Jin Sung, “Heat transfer enhancement by flexible flags clamped vertically in a poiseuille channel flow,” *International Journal of Heat and Mass Transfer* **107**, 391–402 (2017).
- [27] Yuzhen Jin, Chunhui Leng, Zhaokun Wang, Xuming Zhang, and Jingyu Cui, “Enhancing heat transfer in laminar channel flow by tuning the mass distribution of a flexible reed,” *Physics of Fluids* **36** (2024).
- [28] Zepeng Chen, Yingzheng Liu, and Hyung Jin Sung, “Enhancement of heat transfer by a buckled flexible filament in a channel flow,” *International Journal of Heat and Mass Transfer* **224**, 125364 (2024).
- [29] Sung Goon Park, “Heat transfer enhancement by a wall-mounted flexible vortex generator with an inclination angle,” *International Journal of Heat and Mass Transfer* **148**, 119053 (2020).
- [30] Yujia Chen, Jongmin Yang, Yingzheng Liu, and Hyung Jin Sung, “Heat transfer enhancement in a poiseuille channel flow by using multiple wall-mounted flexible flags,” *International Journal of Heat and Mass Transfer* **163**, 120447 (2020).
- [31] Samer Ali, Sébastien Menanteau, Charbel Habchi, Thierry Lemenand, and Jean-Luc Harion, “Heat transfer and mixing enhancement by using multiple freely oscillating flexible vortex generators,” *Applied Thermal Engineering* **105**, 276–289 (2016).
- [32] Lin Ding, Jinzhen Xiong, Yuxiong Han, Zheyu Zhu, and Jingyu Ran, “Improvement of mixing performance in laminar micromixers utilizing vortex-induced vibration of two circular cylinders,” *International Communications in Heat and Mass Transfer* **159**, 108285 (2024).

- [33] Xiang Zhang, Guowei He, and Xing Zhang, “Fluid–structure interactions of single and dual wall-mounted 2d flexible filaments in a laminar boundary layer,” *Journal of Fluids and Structures* **92**, 102787 (2020).
- [34] George M Hughes, “Morphometrics of fish gills,” *Respiration Physiology* **14**, 1–25 (1972).
- [35] Chengyu Li, Haibo Dong, and Kai Zhao, “A balance between aerodynamic and olfactory performance during flight in drosophila,” *Nature communications* **9**, 3215 (2018).
- [36] Zhipeng Lou, Menglong Lei, Haibo Dong, and Chengyu Li, “Wing–antenna interaction reduces odour fatigue in butterfly odour-tracking flight,” *Journal of Fluid Mechanics* **998**, A45 (2024).
- [37] Jacob M Peters, Orit Peleg, and L Mahadevan, “Collective ventilation in honeybee nests,” *Journal of The Royal Society Interface* **16**, 20180561 (2019).
- [38] William Gilpin, Matthew Storm Bull, and Manu Prakash, “The multiscale physics of cilia and flagella,” *Nature Reviews Physics* **2**, 74–88 (2020).
- [39] Michael J Shelley, “Flows, self-organization, and transport in living cells,” *Physical Review Fluids* **9**, 120501 (2024).
- [40] Jaap den Toonder, Femke Bos, Dick Broer, Laura Filippini, Murray Gillies, Judith de Goede, Titie Mol, Mireille Reijme, Wim Talen, Hans Wilderbeek, *et al.*, “Artificial cilia for active micro-fluidic mixing,” *Lab on a Chip* **8**, 533–541 (2008).
- [41] AR Shields, BL Fiser, EE Evans, MR Falvo, S Washburn, and R Superfine, “Biomimetic cilia arrays generate simultaneous pumping and mixing regimes,” *Proceedings of the National Academy of Sciences* **107**, 15670–15675 (2010).
- [42] Yusheng Wang, Saksham Sharma, Fabien Maldonado, and Xiaoguang Dong, “Wirelessly actuated ciliary airway stent for excessive mucus transportation,” *Advanced materials technologies* **8**, 2301003 (2023).
- [43] Hao-Bo Zhao, Chao-Ben Zhao, Quan Zhou, and Kai Leong Chong, “Thermal convection modulated by actively oscillating filament: The effect of filament rigidity,” *International Journal of Heat and Mass Transfer* **228**, 125649 (2024).
- [44] Thien-Binh Nguyen, Dongdong Liu, Harshal Raut, Amitabh Bhattacharya, Atul Sharma, and Tuan Tran, “Enhancement of convective heat transfer using magnetically flapping fin array,” *International Communications in Heat and Mass Transfer* **129**, 105638 (2021).
- [45] Pengyong Xie and Xiaobing Zhang, “A novel method of enhancing convective heat transfer by dynamic controlling rib,” *International Communications in Heat and Mass Transfer* **119**, 104830 (2020).
- [46] Michel Y Jaffrin, “Hydrodynamic techniques to enhance membrane filtration,” *Annual Review of Fluid Mechanics* **44**, 77–96 (2012).
- [47] Andy J Turko, Bianca Cisternino, and Patricia A Wright, “Calcified gill filaments increase respiratory function in fishes,” *Proceedings of the Royal Society B* **287**, 20192796 (2020).
- [48] James A Strother, “Hydrodynamic resistance and flow patterns in the gills of a tilapine fish,” *Journal of Experimental Biology* **216**, 2595–2606 (2013).
- [49] Alexander J Smits, “Undulatory and oscillatory swimming,” *Journal of Fluid Mechanics* **874**, P1 (2019).

- [50] Peter A Dewey, Antoine Carriou, and Alexander J Smits, “On the relationship between efficiency and wake structure of a batoid-inspired oscillating fin,” *Journal of fluid mechanics* **691**, 245–266 (2012).
- [51] Keith W Moored, Peter A Dewey, AJ Smits, and H Haj-Hariri, “Hydrodynamic wake resonance as an underlying principle of efficient unsteady propulsion,” *Journal of Fluid Mechanics* **708**, 329–348 (2012).
- [52] James HJ Buchholz and Alexander J Smits, “On the evolution of the wake structure produced by a low-aspect-ratio pitching panel,” *Journal of fluid mechanics* **546**, 433–443 (2006).
- [53] Haibo Dong, Rajat Mittal, Meliha Bozkurttas, and Fady Najjar, “Wake structure and performance of finite aspect-ratio flapping foils,” in *43rd AIAA aerospace sciences meeting and exhibit* (2005) p. 81.
- [54] Teis Schnipper, Anders Andersen, and Tomas Bohr, “Vortex wakes of a flapping foil,” *Journal of Fluid Mechanics* **633**, 411–423 (2009).
- [55] T Van Buren, D Floryan, D Brunner, U Senturk, and AJ Smits, “Impact of trailing edge shape on the wake and propulsive performance of pitching panels,” *Physical Review Fluids* **2**, 014702 (2017).
- [56] Peter D Yeh, Yuanda Li, and Alexander Alexeev, “Efficient swimming using flexible fins with tapered thickness,” *Physical Review Fluids* **2**, 102101 (2017).
- [57] Brian Dean and Bharat Bhushan, “Shark-skin surfaces for fluid-drag reduction in turbulent flow: a review,” *Philosophical Transactions of the Royal Society A: Mathematical, Physical and Engineering Sciences* **368**, 4775–4806 (2010).
- [58] Yilmaz Bayazit, Eph M Sparrow, and Daniel D Joseph, “Perforated plates for fluid management: Plate geometry effects and flow regimes,” *International Journal of Thermal Sciences* **85**, 104–111 (2014).
- [59] Tom Marzin, Kerian Le Hay, Emmanuel de Langre, and Sophie Ramanarivo, “Flow-induced deformation of kirigami sheets,” *Physical Review Fluids* **7**, 023906 (2022).
- [60] Jing Li, Ranjiangshang Ran, Haihuan Wang, Yuchen Wang, You Chen, Shichao Niu, Paulo E Arratia, and Shu Yang, “Aerodynamics-assisted, efficient and scalable kirigami fog collectors,” *Nature communications* **12**, 5484 (2021).
- [61] Karan Kakroo and Hamid Sadat, “High-fidelity fluid–structure interaction simulations of perforated elastic vortex generators,” *Physics of Fluids* **36** (2024).
- [62] M Guttag, Hussain H Karimi, C Falcón, and Pedro M Reis, “Aeroelastic deformation of a perforated strip,” *Physical Review Fluids* **3**, 014003 (2018).
- [63] Yaqing Jin, Jin-Tae Kim, Shyuan Cheng, Oumar Barry, and Leonardo P Chamorro, “On the distinct drag, reconfiguration and wake of perforated structures,” *Journal of Fluid Mechanics* **890**, A1 (2020).
- [64] Vishwa T Kasoju and Arvind Santhanakrishnan, “Aerodynamic interaction of bristled wing pairs in fling,” *Physics of Fluids* **33** (2021).
- [65] Shannon K Jones, Young JJ Yun, Tyson L Hedrick, Boyce E Griffith, and Laura A Miller, “Bristles reduce the force required to ‘fling’ wings apart in the smallest insects,” *Journal of Experimental Biology* **219**, 3759–3772 (2016).
- [66] Eize Stamhuis and William Thielicke, “Pivlab—towards user-friendly, affordable and accurate digital particle image velocimetry in matlab,” *Journal of open research software* **2**, 30 (2014).

- [67] Kouros Shoole and Rajat Mittal, “Computational study of flow-induced vibration of a reed in a channel and effect on convective heat transfer,” *Physics of Fluids* **26** (2014).
- [68] Lawrence F Shampine and Mark W Reichelt, “The matlab ode suite,” *SIAM journal on scientific computing* **18**, 1–22 (1997).
- [69] John R Dormand and Peter J Prince, “A family of embedded runge-kutta formulae,” *Journal of computational and applied mathematics* **6**, 19–26 (1980).
- [70] Sadatoshi Taneda, “Experimental investigation of the wakes behind cylinders and plates at low reynolds numbers,” *Journal of the Physical Society of Japan* **11**, 302–307 (1956).
- [71] Sung Goon Park, Cheong Bong Chang, Boyoung Kim, and Hyung Jin Sung, “Simulation of fluid-flexible body interaction with heat transfer,” *International Journal of Heat and Mass Transfer* **110**, 20–33 (2017).
- [72] S Co R Dennis, JD Hudson, and N Smith, “Steady laminar forced convection from a circular cylinder at low reynolds numbers,” *The Physics of Fluids* **11**, 933–940 (1968).
- [73] Tyson L Hedrick, “Software techniques for two-and three-dimensional kinematic measurements of biological and biomimetic systems,” *Bioinspiration & biomimetics* **3**, 034001 (2008).
- [74] Francois Lekien, Chad Coulliette, Arthur J Mariano, Edward H Ryan, Lynn K Shay, George Haller, and Jerry Marsden, “Pollution release tied to invariant manifolds: A case study for the coast of florida,” *Physica D: Nonlinear Phenomena* **210**, 1–20 (2005).
- [75] Manikandan Mathur, George Haller, Thomas Peacock, Jori E Ruppert-Felsot, and Harry L Swinney, “Uncovering the lagrangian skeleton of turbulence,” *Physical Review Letters* **98**, 144502 (2007).
- [76] J Peng and JO Dabiri, “Transport of inertial particles by lagrangian coherent structures: application to predator-prey interaction in jellyfish feeding,” *Journal of Fluid Mechanics* **623**, 75–84 (2009).
- [77] Zixuan Wu, Saikat Basu, Seungho Kim, Mark Sorrells, Francisco J Beron-Vera, and Sunghwan Jung, “Coherent spore dispersion via drop-leaf interaction,” *Science advances* **10**, eadj8092 (2024).
- [78] George Haller, “Lagrangian coherent structures,” *Annual review of fluid mechanics* **47**, 137–162 (2015).
- [79] Shawn C Shadden, Francois Lekien, and Jerrold E Marsden, “Definition and properties of lagrangian coherent structures from finite-time lyapunov exponents in two-dimensional aperiodic flows,” *Physica D: Nonlinear Phenomena* **212**, 271–304 (2005).
- [80] George Haller and Guocheng Yuan, “Lagrangian coherent structures and mixing in two-dimensional turbulence,” *Physica D: Nonlinear Phenomena* **147**, 352–370 (2000).
- [81] Steven L Brunton and Clarence W Rowley, “Fast computation of finite-time lyapunov exponent fields for unsteady flows,” *Chaos: An Interdisciplinary Journal of Nonlinear Science* **20** (2010).
- [82] Shawn C Shadden, John O Dabiri, and Jerrold E Marsden, “Lagrangian analysis of fluid transport in empirical vortex ring flows,” *Physics of fluids* **18** (2006).
- [83] Greg A Voth, G Haller, and Jerry P Gollub, “Experimental measurements of stretching fields in fluid mixing,” *Physical review letters* **88**, 254501 (2002).
- [84] M Liu, FJ Muzzio, and RL Peskin, “Quantification of mixing in aperiodic chaotic flows,” *Chaos, Solitons & Fractals* **4**, 869–893 (1994).

- [85] MARIA GRAZIA Badas, Federico Domenichini, and Giorgio Querzoli, “Quantification of the blood mixing in the left ventricle using finite time Lyapunov exponents,” *Meccanica* **52**, 529–544 (2017).
- [86] Francisco J Beron-Vera, María J Olascoaga, and Gustavo J Goni, “Surface ocean mixing inferred from different multisatellite altimetry measurements,” *Journal of physical oceanography* **40**, 2466–2480 (2010).
- [87] Ruth A Lambert and Roger H Rangel, “The role of elastic flap deformation on fluid mixing in a microchannel,” *Physics of Fluids* **22** (2010).
- [88] Prashant Saini, Atul Dhar, and Satvasheel Powar, “Performance enhancement of fin and tube heat exchanger employing curved trapezoidal winglet vortex generator with circular punched holes,” *International Journal of Heat and Mass Transfer* **209**, 124142 (2023).
- [89] Daniel B Quinn, George V Lauder, and Alexander J Smits, “Scaling the propulsive performance of heaving flexible panels,” *Journal of fluid mechanics* **738**, 250–267 (2014).
- [90] Leo Liu, Qiang Zhong, Tianjun Han, Keith W Moored, and Daniel B Quinn, “Fine-tuning near-boundary swimming equilibria using asymmetric kinematics,” *Bioinspiration & Biomimetics* **18**, 016011 (2022).
- [91] Jessica K Shang, Howard A Stone, and AJ Smits, “Flow past finite cylinders of constant curvature,” *Journal of Fluid Mechanics* **837**, 896–915 (2018).
- [92] Keunhwan Park, Wonjung Kim, and Ho-Young Kim, “Optimal lamellar arrangement in fish gills,” *Proceedings of the National Academy of Sciences* **111**, 8067–8070 (2014).